



An adaptive vibrational resonance method based on cascaded varying stable-state nonlinear systems and its application in rotating machine fault detection

Lei Xiao · Rusmir Bajric · Jingsong Zhao · Junxuan Tang · Xinghui Zhang

Received: 6 December 2019 / Accepted: 5 December 2020 / Published online: 6 January 2021
© The Author(s), under exclusive licence to Springer Nature B.V. part of Springer Nature 2021

Abstract A weak character signal with low frequency can be detected based on the mechanism of vibrational resonance (VR). The detection performance of VR is determined by the synergy of a weak low-frequency input signal, an injected high-frequency sinusoidal interference and the nonlinear system(s). In engineering applications, there are many weak fault signals with high character frequencies. These fault signals are usually submerged in strong background noise. To detect these weak signals, an adaptive detection method for a weak high-frequency fault signal is proposed in this paper. This method is based on the mechanics of VR and cascaded varying stable-state nonlinear systems (VSSNSs). Partial background noise with high frequency is regarded as a special type of high-frequency interference and an

energy source that protrudes a weak fault signal. In this way, high-frequency background noise is utilized in a VSSNS. To improve the detection ability, manually generated high-frequency interference is injected into another VSSNS. The VSSNS can be transformed into a monostable state, bistable state or tristable state by tuning the system parameters. The proposed method is validated by a simulation signal and industrial applications. The results show the effectiveness of the proposed method to detect a weak high-frequency character signal in engineering problems.

Keywords Vibrational resonance · Varying stable-state nonlinear system · Cascaded nonlinear systems · Weak high-frequency character signal · Rotating machine

L. Xiao (✉) · J. Tang
College of Mechanical Engineering, Donghua University,
Shanghai 201620, China
e-mail: leixiao211@163.com

R. Bajric
E. ON Climate & Renewables UK Limited,
Coventry CV4 8LG, UK

J. Zhao
Army Military Transportation University, Tianjin 300161,
China

X. Zhang
China North Vehicle Research Institute,
Fengtai District, Beijing 100072, China

1 Introduction

Vibrational resonance (VR) is a phenomenon in which the amplification of a weak low-frequency signal can be enhanced by injecting a high-frequency periodic force [1]. This phenomenon shows many similarities to the phenomenon of stochastic resonance (SR), except that the high-frequency periodic force replaces random noise [2]. The mechanics of both VR and SR require noise injection rather than noise cancellation

when detecting a weak low-frequency signal. Here, the high-frequency periodic force in VR can be regarded as special noise. Therefore, both VR and SR can be deemed noise utilization methods.

Traditional VR and SR perform well when detecting a weak signal whose frequency is lower than 1 Hz. However, if the frequency of a weak signal is much greater than 1 Hz, improvements are needed due to the restriction of adiabatic approximate theory. By using the scale transformation method, a high-frequency signal can be transformed into a low-frequency signal [2]. Based on the scale transformation method, Tan et al. [3] proposed a frequency-shifted and rescaling transfer method (FSRTM) and combined it with SR to detect bearing faults. This FSRTM is efficient if the fault characteristic frequency is known in advance. Wang et al. [4] developed an adaptive multiscale noise-tuning SR for diagnosing bearing faults.

An incipient fault in an operating rotating machine causes a typical weak high-frequency character signal with a frequency greater than 1 Hz. Detecting such a weak fault signal is an important issue in engineering applications. Researchers have shown great interest in producing different useful methods, such as spectral kurtosis [5, 6], empirical model decomposition (EDM) [7], wavelet transform [8] and S transform [9]. These methods are known as noise cancellation methods because their main goal is to extract fault-induced signatures by removing or suppressing background noises. Most noise utilization and noise cancellation methods can be regarded as frequency-based methods. In addition to these frequency-based methods, model-based methods are also important tools used in fault reconstruction [10–12].

Qiao et al. [13] stressed that weak fault characteristics can be weakened or even destroyed during the noise cancellation process; thus, they proposed an adaptive unsaturated bistable SR to detect bearing faults. Zhang et al. [14] proposed a nonlinear system resonance method to diagnose bearing faults. Li et al. [15] developed an adaptive SR method based on coupled bistable systems. Dong et al. [16] developed a second-order matched SR to improve the signal-to-noise ratio (SNR) of a weak period signal. Zhang et al. [17] constructed a new exponential bistable potential function in second-order underdamped SR to detect rolling bearing faults. Lai et al. [18] developed a multiparameter-adjusting SR in a standard tristable system. Additional works on SR applications

in rotating machine fault detection are contained in Refs. [19, 20].

The above noise utilization methods for weak fault detection were mainly based on SR [13, 15–20]. Another noise utilization method, VR, is easier to control than SR [21]. The concerns related to added noise intensity, noise type and noise distribution that must be considered in SR need not be considered in VR [22]. Even though VR has been successfully applied to analogue electronic circuits [23, 24], excitable neurons [25, 26] and optical devices [27, 28], its application in weak fault detection on a rotating machine is relatively less common compared to SR. Here, only a limited number of recent and relevant publications are listed below. Gao et al. [29] proposed a VR-based weak fault detection method and compared the detection performance with envelope spectrum analysis. Liu et al. [29] proposed a step-varying VR based on a duffing oscillator nonlinear system to enhance the detection ability of bearing faults. In the methods proposed in Refs. [29, 30], only one nonlinear system was adopted. Xiao et al. [22] constructed an array of nonlinear systems for a VR-based weak fault detection method. In the above detection methods, the classic bistable state potential well function was adopted in nonlinear systems [22, 29, 30].

In addition to the above works, the classic bistable system (CBS) was commonly adopted in most fault detection methods that were based on VR [2, 4, 16, 22, 29, 30]. However, output saturation may occur when adopting a CBS. In addition, only one nonlinear system is adopted in most of the existing VR-based fault detection methods for rotating machines. Even though there are two or more nonlinear systems outlined in some publications, the nonlinear systems are presented in second-order, parallel or coupled formats [14, 17, 18].

Given the above analysis, an adaptive VR method for detecting a high-frequency character signal based on cascaded varying stable-state nonlinear systems (VSSNSs) is proposed for detecting a fault on a rotating machine. The proposed method integrates the following advantages:

- (1) The proposed detection method deploys the easy control advantage of VR compared with SR, since the concerns related to noise intensity, noise type and noise distribution need not be

considered. Furthermore, the FSRTM proposed by Tan et al. [3] is introduced to overcome the restriction of adiabatic approximation theory when processing a high-frequency fault signal.

- (2) Cascaded nonlinear systems use background noise and manually injected high-frequency sinusoidal interference. Different from the existing noise cancellation methods, the background noise is used rather than filtered in our proposed method. Since the frequencies of background noises exist in a wide range, partial noises whose frequencies are very high can be regarded as special energy for resonance in a nonlinear system.
- (3) The potential well function in the nonlinear systems exists in a varying stable state rather than a fixed state; the nonlinear system can be transferred in different stable states by tuning system parameters. Therefore, there are more possibilities for a nonlinear system to achieve resonance.

The above aspects are considered in an integrated manner, which is the main contribution of this paper. The cascaded nonlinear systems that detect a high-frequency character signal are formulated using varying stable-state potential well functions and VR mechanisms. The proposed detection method is oriented to mechanical applications that have heavy strong background noise to enrich the limited number of VR-based fault detection methods in the existing publications.

The rest of the paper is organized as follows: Section 2 introduces the proposed method for detecting a high-frequency character signal. Validation of the proposed method is conducted on different faults of rotating machines in Sect. 3. The detection performance is assessed by using different nonlinear systems in Sect. 4, and the paper is concluded in Sect. 5.

2 Detection method for a high-frequency character signal based on VR

VR occurs when a high-frequency sinusoidal interference of appropriate amplitude can optimally amplify a weak low-frequency periodic signal in a nonlinear system. Let $s(t)$ and $I(t)$ represent the weak periodic signal and high-frequency sinusoidal interference,

respectively. The frequency of the weak signal is usually lower than 1 Hz. The governing equation in VR is as follows:

$$\frac{dx}{dt} = -\frac{dU(x)}{dx} + s(t) + I(t) \tag{1}$$

where $s(t) = A\cos\omega t$, and the amplitude and frequency of the weak periodic signal are A and $\omega/2\pi$. $I(t) = B\cos\Omega t$, the amplitude and frequency of the high-frequency sinusoidal interference are B and $\Omega/2\pi$, respectively. $\Omega \gg 2\pi$. $U(x)$ is the potential well function in the nonlinear system.

2.1 Saturation phenomenon in a CBS

In classic VR, the nonlinear system is a CBS. Its potential well function can be written as

$$U(x) = -\frac{a_c}{2}x^2 + \frac{b_c}{4}x^4, \quad a_c, b_c > 0 \tag{2}$$

where a_c and b_c are the system parameters in the CBS. Without external interference, the CBS has two potential wells with bottoms located at $\pm x_s = \pm\sqrt{a_c/b_c}$ and one unstable point located at $x_u = 0$. The height of the barrier is $\Delta U = a_c^2/4b_c$.

Assuming there is no input force in the CBS (i.e., $A = 0$ and $B = 0$), the output x can be calculated by substituting Eq. (2) into Eq. (1) according to the Bernoulli differential equation, and Eq. (3) is obtained. Considering two situations, $t = 0$ and $t \rightarrow +\infty$, the output x is given in Eq. (4).

$$x = \pm\sqrt{\frac{a_c \exp(2a_c t)}{1 + b_c \exp(2a_c t)}} \tag{3}$$

$$x = \begin{cases} \pm\sqrt{a_c/(1 + b_c)} & t = 0 \\ \pm\sqrt{a_c/b_c} & t \rightarrow +\infty \end{cases} \tag{4}$$

From Eqs. (3) and (4), the absolute values of the output x are limited in a range between $\sqrt{a_c/(1 + b_c)}$ and $\sqrt{a_c/b_c}$. A simplified illustration is given in Fig. 1, where different system parameters are considered. In Fig. 1, no matter what values these parameters are set to, $\text{abs}(x)$ always asymptotically approaches a fixed value with the continuous increase in time t . For example, when $a_c = 1$ and $b_c = 3$, $\text{abs}(x)$ approaches 0.57 as time t increases. This phenomenon is caused by the intrinsic characteristic of a CBS and is defined as

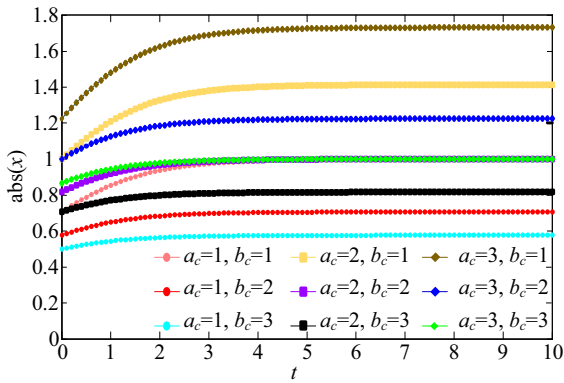


Fig. 1 Output saturation phenomenon in a CBS

output saturation. The output signal x varies with the input signals accordingly. Once the output signal x reaches a certain value, the output saturation phenomenon is about to occur.

2.2 The construction of a VSSNS

Since a CBS may generate output saturation, the detection ability is thus restricted. In addition, the fixed stable state may need more time for system parameter adjustment to achieve resonance. Therefore, a reflection-symmetric sextic potential well function is adopted as

$$U(x) = \frac{1}{6a}x^6 - \frac{1+b}{20}x^4 + \frac{b}{2}x^2 \tag{5}$$

where a and b are the system parameters in a VSSNS. We set a to a positive real value, but b can be an arbitrary real value.

If $\frac{dU(x)}{dx} = 0$, Eq. (5) can be rewritten as

$$x\left(\frac{1}{a}x^4 - \frac{1+b}{5}x^2 + b\right) = 0 \tag{6}$$

One of the real roots of Eq. (6) is $x = 0$.

$\frac{1}{a}x^4 - \frac{1+b}{5}x^2 + b = 0$ can be rewritten as

$$5x^4 + 0x^3 - a(1+b)x^2 + 0x + 5ab = 0 \tag{7}$$

The root discriminant Δ of Eq. (7) is calculated as

$$\begin{cases} a_x = 5, & b_x = 0, & c_x = -a(1+b), & d_x = 0, & e_x = 5ab \\ E_1 = 3b_x^2 - 8a_xc_x \\ E_2 = -b_x^3 + 4a_xb_xc_x - 8a_x^2d_x \\ E_3 = 3b_x^4 + 16a_x^2c_x^2 - 16a_xb_x^2c_x + 16a_x^2b_xd_x - 64a_x^3e_x \\ \Delta_1 = E_1^2 - 3E_3 \\ \Delta_2 = E_1E_3 - 9E_2^2 \\ \Delta_3 = E_3^2 - 3E_1E_2^2 \\ \Delta = \Delta_2^2 - 4\Delta_1\Delta_3 \end{cases} \tag{8}$$

Under the synergistic effects of the input signal, the outer force and the system parameters, the potential well function shows different stable states. Therefore, the resonance ability is enhanced by employing the VSSNS. Here, a simplified example is given in Fig. 2 with the following parameters: $a = 20$, $b = -4$, $b = 1$, and $b = 4$. In Fig. 2, the stable-state types of the VSSNS are bistable ($b = -4$), monostable ($b = 1$) and tristable ($b = 4$). Furthermore, if system parameter a is set to a constant (here a is set to 20) but b is changed from -4 to 4, the potential well of the VSSNS is changed accordingly, and the stable-state types of the VSSNS are changed as follows: bistable \rightarrow monostable \rightarrow tristable.

If high-frequency interference is considered, let $x(t) = X(t) + \Psi(\tau, \Omega t)$, where $X(t)$ and $\Psi(t)$ are slow and fast variables according to Ref. [31]. Assume that the mean value of Ψ , $\langle \Psi \rangle$, with respect to time $\tau = \Omega t$ is

$$\langle \psi \rangle = \frac{1}{2\pi} \int_0^{2\pi} \psi d\tau \tag{9}$$

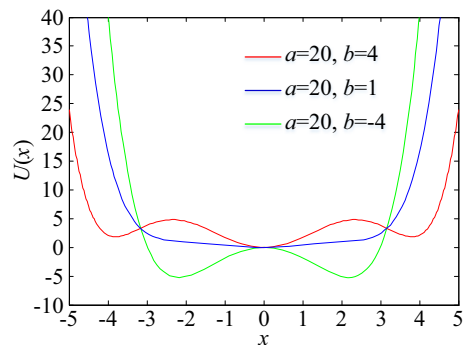
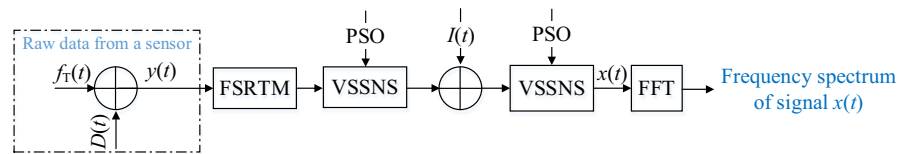


Fig. 2 Illustration of potential well functions with different system parameters

Fig. 3 The procedure of the proposed VR-based detection method



$$\langle \psi^m \rangle = \frac{1}{2\pi} \int_0^{2\pi} \psi^m d\tau \tag{10}$$

The equation for the slow motion can be regarded as the equation of the motion of a system with the effective potential well function as

$$U_{\text{eff}}(X) = \frac{1}{2}R_1X^2 + \frac{1}{4}R_2X^4 + \frac{1}{6a}X^6 \tag{11}$$

where

$$\begin{cases} R_1 = b^2 - \frac{3(1+b)B^2}{10\Omega^4} + \frac{15B^4}{8a\Omega^4} \\ R_2 = -\frac{1+b}{5} + \frac{5B^2}{a\Omega^4} \end{cases} \tag{12}$$

The equilibrium points for the slow motion are given by

$$\begin{cases} X_1^* = 0 \\ X_{2,3}^* = \pm \left(\frac{-a^2R_2 + \sqrt{a^2R_2^2 - 4aR_1}}{2a} \right)^{1/2} \\ X_{4,5}^* = \pm \left(\frac{-a^2R_2 - \sqrt{a^2R_2^2 - 4aR_1}}{2a} \right)^{1/2} \end{cases} \tag{13}$$

When $X^* \neq 0$, let $Y = X - X^*$ where $Y = A_L \cos(\omega t + \Phi)$ in the limit $t \rightarrow \infty$. If the nonlinear terms are neglected, A_L and the response amplitude Q are obtained as

$$A_L = \frac{A}{\sqrt{w_r^2 + w^2}} \tag{14}$$

$$w_r^2 = R_1 + 3R_2X^{*2} + \frac{5}{a}X^{*4} \tag{15}$$

$$Q = \frac{A_L}{A} = \frac{1}{\sqrt{w_r^2 + w^2}} \tag{16}$$

2.3 The detection method for a weak high-frequency character signal

The original VR method only focuses on the detection of a weak signal whose frequency is much lower than 1 Hz due to the restriction of the adiabatic approximation theory. However, the frequency of a weak target signal is usually greater than 1 Hz in engineering circumstances. Here, FSRTM is adopted to overcome the restriction of the adiabatic approximation theory.

The flowchart of the proposed VR-based detection method is illustrated in Fig. 3, where the raw data from a sensor contain the weak high-frequency character signal $f_T(t)$ and background noise $D(t)$. Here, $f_T(t)$ is defined to distinguish the difference between a weak high-frequency character signal and a weak low-frequency input signal ($s(t)$). The weak high-frequency character signal $f_T(t)$ after processing by FSRTM can be regarded as a weak periodic signal $s(t)$; however, the frequency of $f_T(t)$ before processing by FSRTM is much higher than that of $s(t)$. The mixed signal $y(t)$, which contains background noise, is processed by FSRTM and then imported into cascaded nonlinear systems with varying stable states. In this first VSSNS, the high-frequency background noise is regarded as the high-frequency interference for resonance. In the second VSSNS, manually injected high-frequency sinusoidal interference is used for resonance. In the two VSSNSs, particle swarm optimization (PSO) is adopted to optimize the system parameters along with the parameters of the injected high-frequency interference. The output from the second VSSNS is processed by fast Fourier transform (FFT); consequently, the frequency of the output signal can be obtained, and the high-frequency character signal can be detected by comparing the resonated frequency with the target frequency.

Note that the frequencies of the background noises usually exist in a wide range. Some of the frequencies are very high, but some are low. Even though FSRTM is conducted on the mixed signal that contains the

target signal and the background noise, the frequencies of some noises are still very high after processing by FSRTM. Therefore, the noises whose frequencies are very high even after processing by FSRTM can be regarded as the high-frequency interference for resonance, and it is unnecessary to inject a high-frequency interference into the first VSSNS.

The fourth-order Runge–Kutta discretization method is used to calculate the discretized output from the two VSSNSs as Eq. (17), where h is the time calculation step, which is usually the reciprocal of the sampling frequency (f_s). Note that h should be recalculated due to the rescaling process in the FSRTM. $P[n]$ and $O[n]$ are the discretization forms of $P(t)$ and $O(t)$. $P(t)$ is the data before processing in a VSSNS, and $O(t)$ is the output data from the VSSNS. n is the data series.

$$\begin{cases} k_1 = h \left(-\frac{1}{a} O[n]^5 + \frac{(1+b)}{5} O[n]^3 - b O[n] + P[n] \right) \\ k_2 = h \left(\left(-\frac{1}{a} O[n] + \frac{k_1}{2} \right)^5 + \left(\frac{1+b}{5} O[n] + \frac{k_1}{2} \right)^3 - b \left(O[n] + \frac{k_1}{2} \right) + P[n] \right) \\ k_3 = h \left(\left(-\frac{1}{a} O[n] + \frac{k_2}{2} \right)^5 + \left(\frac{1+b}{5} O[n] + \frac{k_2}{2} \right)^3 - b \left(O[n] + \frac{k_2}{2} \right) + P[n] \right) \\ k_4 = h \left(\left(-\frac{1}{a} O[n] + k_3 \right)^5 + \left(\frac{1+b}{5} O[n] + k_3 \right)^3 - b (O[n] + k_3) + P[n] \right) \\ O[n+1] = O[n] + \frac{1}{6} (k_1 + k_2 + k_3 + k_4) \end{cases} \quad (17)$$

function. Here, the objective is to maximize the SNR of a target signal defined as

$$\text{SNR} = 10 \log_{10} \frac{\eta_T^2}{\eta^2 - \eta_T^2} \quad (18)$$

where η is the FFT amplitude of the output from a nonlinear system; η_T is the FFT amplitude of the resonated frequency. Note that the definition of SNR is not standard in Eq. (18). To avoid the impact caused by the positive or negative values of the amplitudes of the target signal and noise, the square operator is utilized in Eq. (18).

Since there is no general guidance or theoretical standard about the parameter settings of a high-frequency interference in VR, the amplitude and frequency of a high-frequency interference signal is

2.4 Parameter optimization by PSO

The resonance phenomenon and the stable type of a VSSNS are determined by the system parameters and the high-frequency interference. As shown in Fig. 3, PSO is adopted twice to optimize the system parameters in VSSNSs and the parameters of the injected high-frequency interference in the second VSSNS. PSO is a random searching algorithm and does not require the gradient information of an objective

empirically set to be more than 100 times greater than the amplitude and frequency of the target signal according to Refs. [21, 22, 32, 33]. PSO is adopted to optimize the frequency and amplitude of an injected high-frequency interference.

When optimizing the system parameters in the first VSSNS, a particle is constructed with two dimensions that represent the calculation of parameters a and b . Some basic settings for PSO are given, including the positions and velocities of particles along with their associated maximum and minimum values, the

population size of particles (P_{size}), terminal iteration epoch (T_{gen}) and learning factors C_1 and C_2 .

The velocities and positions of particles are updated according to Eqs. (19–20).

$$\begin{cases} V_{a,i} = V_{a,i-1} + C_1 \times \sigma_{1,i} \times (L_{a,i-1} - P_{a,i-1}) + C_2 \times \sigma_{2,i} \times (G_{a,i-1} - P_{a,i-1}) \\ V_{b,i} = V_{b,i-1} + C_1 \times \sigma_{1,i} \times (L_{b,i-1} - P_{b,i-1}) + C_2 \times \sigma_{2,i} \times (G_{b,i-1} - P_{b,i-1}) \end{cases} \quad (19)$$

second VSSNS, a particle has four dimensions that represent the system parameters a and b and the amplitude B and frequency F of an injected high-frequency interference signal where $2\pi F = \Omega$. The

$$\begin{cases} P_{a,i} = P_{a,i-1} + V_{a,i} \\ P_{b,i} = P_{b,i-1} + V_{b,i} \end{cases} \quad (20)$$

velocities and positions of the particles in the second VSSNS are updated according to Eqs. (21–22).

$$\begin{cases} V_{a,i} = V_{a,i-1} + C_1 \times \sigma_{1,i} \times (L_{a,i-1} - P_{a,i-1}) + C_2 \times \sigma_{2,i} \times (G_{a,i-1} - P_{a,i-1}) \\ V_{b,i} = V_{b,i-1} + C_1 \times \sigma_{1,i} \times (L_{b,i-1} - P_{b,i-1}) + C_2 \times \sigma_{2,i} \times (G_{b,i-1} - P_{b,i-1}) \\ V_{B,i} = V_{B,i-1} + C_1 \times \sigma_{1,i} \times (L_{B,i-1} - P_{B,i-1}) + C_2 \times \sigma_{2,i} \times (G_{B,i-1} - P_{B,i-1}) \\ V_{F,i} = V_{F,i-1} + C_1 \times \sigma_{1,i} \times (L_{F,i-1} - P_{F,i-1}) + C_2 \times \sigma_{2,i} \times (G_{F,i-1} - P_{F,i-1}) \end{cases} \quad (21)$$

In Eqs. (19–20), $V_{a,i}$ is the velocity of parameter a in the i th iteration; σ_1 and σ_2 are the random values in the interval of (0, 1); $L_{a,i}$ is the local best parameter a in the i th iteration; $G_{a,i}$ is the global best parameter a in the i th iteration; and $P_{a,i}$ is the current position of parameter a in the i th iteration. $V_{b,i}$, $L_{b,i}$, $G_{b,i}$ and $P_{b,i}$ are the velocity of parameter b , the local best parameter b , the global best parameter b and the current position of parameter b in the i th iteration. If the position or velocity of a parameter exceeds its predetermined upper or lower bound, a new value is generated and replaces the unqualified value.

The terminal condition of optimization is that the optimal SNR is unchanged in the continued T_{gen} iterations. Once the terminal condition is met, the output from the first VSSNS is mixed with an injected high-frequency interference and then imported into the second VSSNS. During the optimization in the

$$\begin{cases} P_{a,i} = P_{a,i-1} + V_{a,i} \\ P_{b,i} = P_{b,i-1} + V_{b,i} \\ P_{B,i} = P_{B,i-1} + V_{B,i} \\ P_{F,i} = P_{F,i-1} + V_{F,i} \end{cases} \quad (22)$$

In Eqs. (21–22), $V_{B,i}$ is the velocity of B in the i th iteration; σ_1 and σ_2 are the random values in the interval of (0, 1); $L_{B,i}$ is the local best B in the i th iteration; $G_{B,i}$ is the global best B in the i th iteration; and $P_{B,i}$ is the current position of B in the i th iteration. $V_{F,i}$, $L_{F,i}$, $G_{F,i}$ and $P_{F,i}$ are the velocity of parameter F , the local best parameter F , the global best parameter F and the current position of parameter F in the i th iteration, respectively. If the position or velocity of a parameter exceeds its upper or lower bound, a new value is generated and replaces the unqualified one. The optimization terminal condition in the second VSSNS is the same as that in the first VSSNS. After optimization, the optimal output signal from the

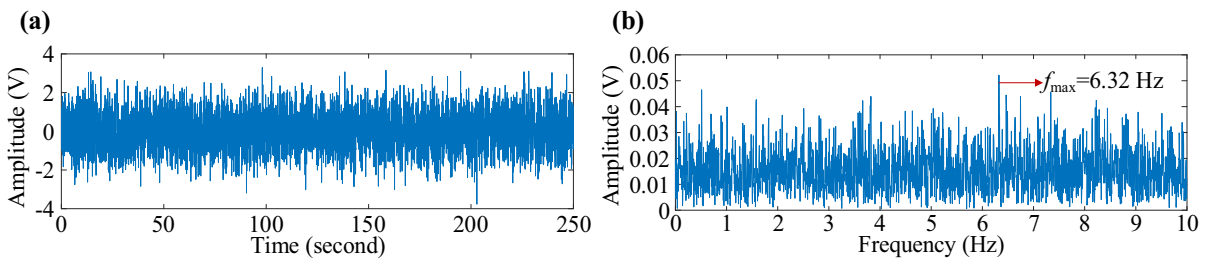


Fig. 4 **a** Time-domain waveform and **b** FFT frequency spectrum of $y(t)$

Table 1 Particle settings in the simulation dataset

Settings	Bound	a	b	B (m/s ²)	F (Hz)
Position	Upper	30	10	500	1000
	Lower	0	- 10	100	500
Velocity	Upper	2	2	50	100
	Lower	- 2	- 2	- 50	- 100

second VSSNS is adapted by FFT to determine the resonated frequency.

3 Validation by a simulation dataset and faults on rotating machines

3.1 Validation by a simulation dataset

A simulation signal is generated, which is $y(t) = 0.1 \times \sin(2\pi \times 0.02t) + D(t)$, where $D(t)$ is additive

white Gaussian noise with an intensity of 1.5 V. The amplitude and frequency of the target signal are 0.1 V and 0.02 Hz, respectively. The sampling frequency f_s is set to 20 Hz. The sampling lasts 250 s. The time-domain waveform and FFT frequency spectrum of $y(t)$ are shown in Fig. 4, where the target frequency 0.02 Hz is submerged in the strong background noise. The frequency with the maximum FFT amplitude (A_{FFT}), which is marked by f_{max} , is 6.32 Hz. The SNR of the target signal (SNR_{FFT}), which is calculated according to Eq. (18) as $- 27.30$ dB.

Since the frequency of the target signal is lower than 1 Hz, FSRTM is unnecessary. However, PSO is adopted to optimize the system parameters and the amplitude and frequency of the injected high-frequency interference. The basic settings are given as follows: $P_{\text{size}} = 30$, $T_{\text{gen}} = 20$, and $C_1 = C_2 = 1.5$. The rest of the settings are listed in Table 1.

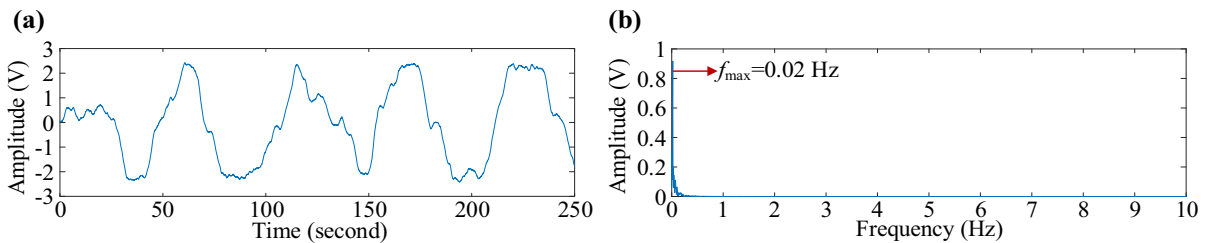


Fig. 5 **a** Time-domain waveform and **b** FFT frequency spectrum of the output signal from our proposed method

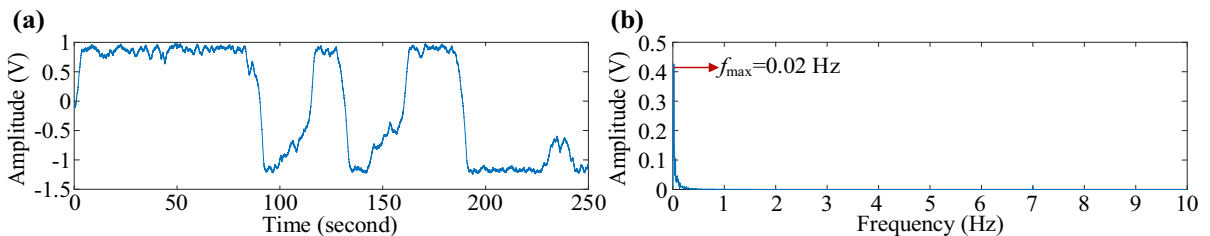


Fig. 6 **a** Time-domain waveform and **b** FFT frequency spectrum of the output signal if the VSSNSs are replaced by the CBSs

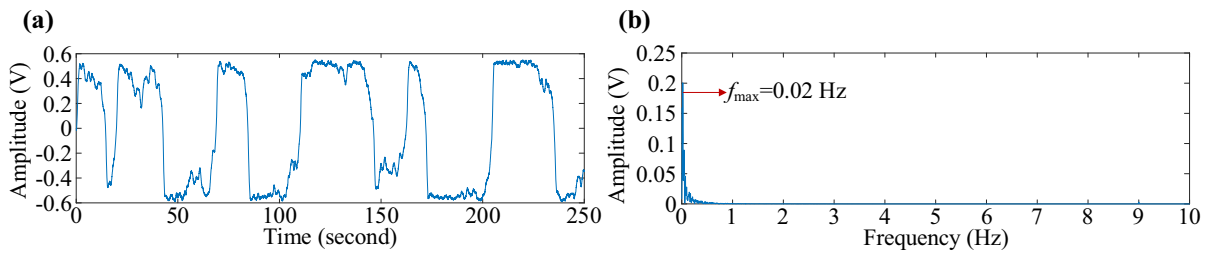


Fig. 7 **a** Time-domain waveform and **b** FFT frequency spectrum of the output signal if only one CBS is adopted

Table 2 Results from different nonlinear systems for the simulation dataset

Comparison criteria	Raw signal	Cascade VSSNSs	Cascade CBSs	One CBS
A_{FFT} (V)	0.038	0.92	0.43	0.20
SNR_{FFT} (dB)	- 27.30	- 0.36	- 3.26	- 4.92

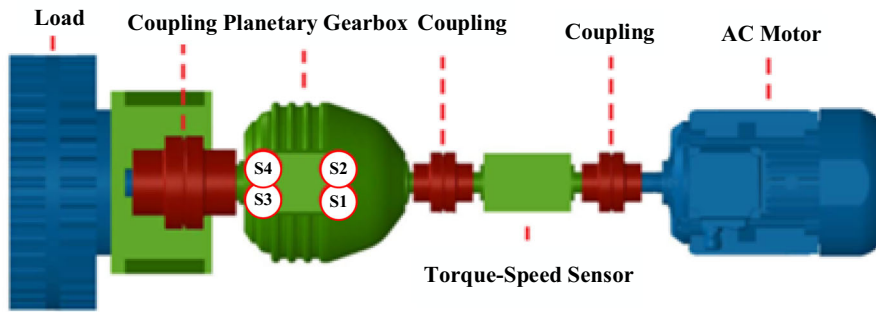


Fig. 8 Schematic of the planetary gearbox test rig

The output signal $x(t)$ from the second VSSNS is shown in Fig. 5, where the target frequency 0.02 Hz is obvious from the perspective of the frequency spectrum. The A_{FFT} of the target frequency is 0.92 V, and the SNR_{FFT} is - 0.36 dB. The optimal parameters are as follows: $a = 20.88$, $b = 0.67$, $B = 390$ V and $F = 789$ Hz. According to parameters a and b , the VSSNS is monostable.

To compare the detection performance using the VSSNSs, each VSSNS in our proposed method is replaced by a CBS. After PSO optimization, the output signal from the second CBS is shown in Fig. 6, where the target frequency is detected with A_{FFT} 0.43 V, and the SNR_{FFT} is - 3.26 dB. The optimal parameters are $a_c = 0.66$, $b_c = 0.93$, $B = 286$ V and $F = 767$ Hz.

In the above comparison, two CBSs are adopted in cascaded format. As analyzed in the Introduction, some researchers have successfully detected target

signals based on VR and only one CBS. To demonstrate the detection performance by using only one CBS and VR, another comparison example is given. After PSO optimization, the output signal is shown in Fig. 7. In Fig. 7, the target signal is detected. The A_{FFT} and SNR_{FFT} of the target frequency are 0.20 V and - 4.92 dB. The optimal parameters are $a_c = 1.79$, $b_c = 8.69$, $B = 227$ V and $F = 809$ Hz.



Fig. 9 The implanted fault on the sun gear

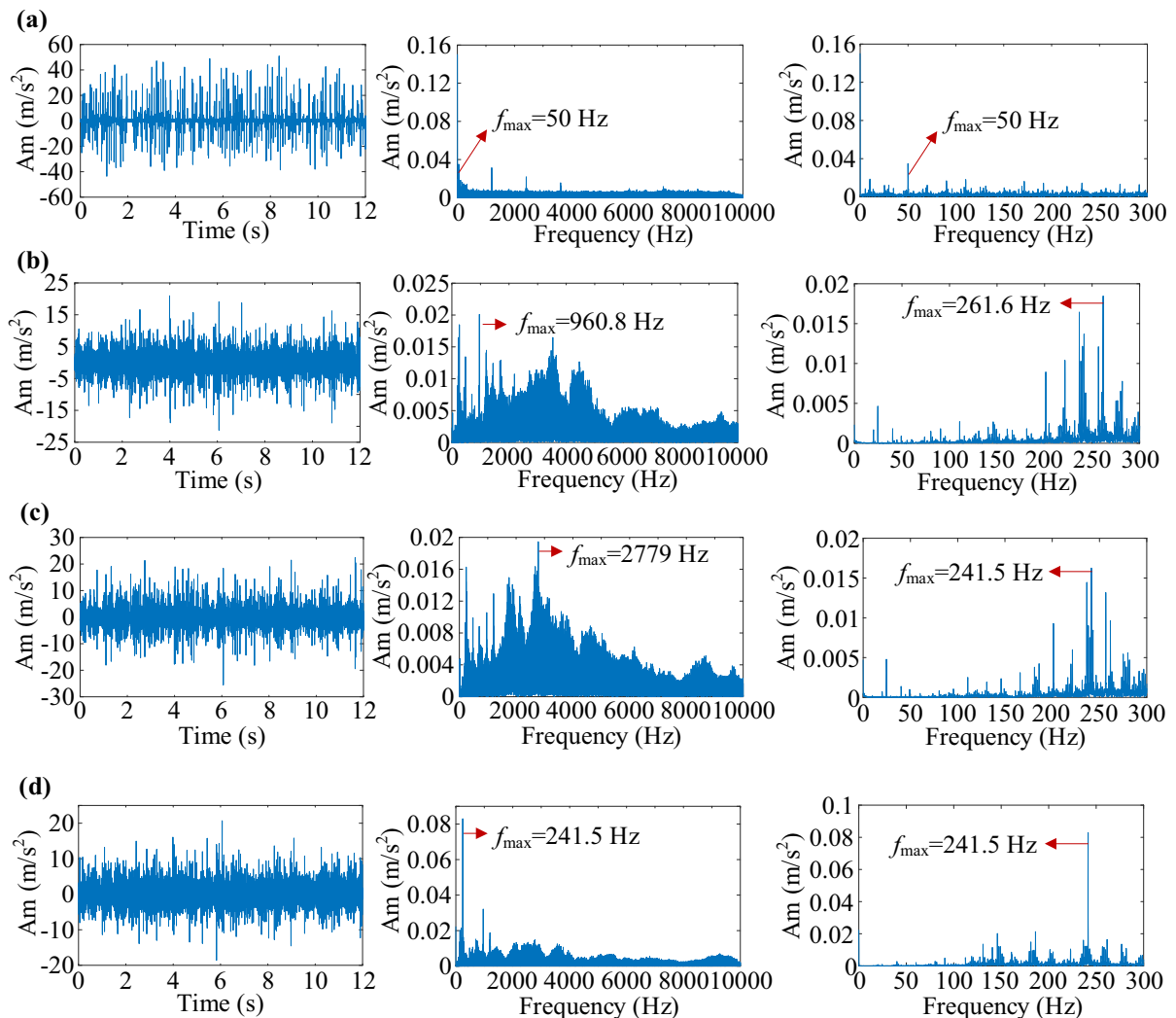


Fig. 10 The time-domain waveforms, FFT spectra and zoomed spectra of the sun gear data collected from **a** S1, **b** S2, **c** S3 and **d** S4

Table 3 Partial PSO settings for detecting rotating machine faults

Settings	Bound	a	b	B (m/s ²)	F (Hz)
Position	Upper	30	10	500	10,000
	Lower	0	-10	100	5000
Velocity	Upper	2	2	50	100
	Lower	-2	-2	-50	-100

In the above comparison examples, the target frequency of 0.02 Hz is detected by adopting different nonlinear system(s), but by adopting our proposed method, the target frequency shows the highest A_{FFT}

along with the maximum SNR_{FFT} . The detection results are compared in Table 2.

3.2 Validation by a gear fault on a planetary gearbox

A dataset for an implanted gear fault is used for validation. It is well known that the vibration sources in a planetary gearbox are very complex due to the meshing among different components. Therefore, the detection of a weak fault in a planetary gearbox is complex and difficult. The schematic of a planetary gearbox test rig is given in Fig. 8, which includes a single-stage planetary gearbox, a 4-kW three-phase

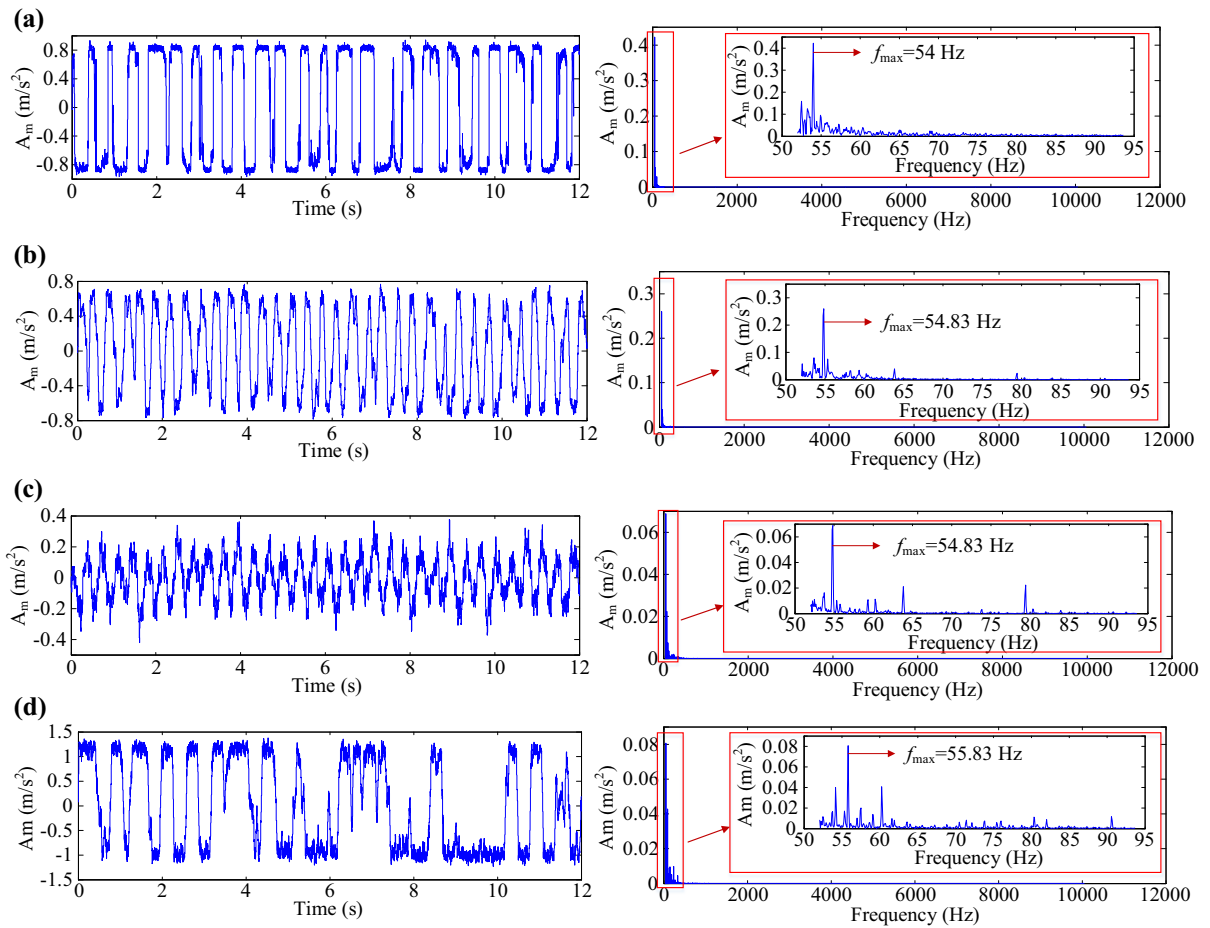


Fig. 11 The time-domain waveforms and FFT spectra of the output signals from the second VSSNS using the data from **a** S1, **b** S2, **c** S3 and **d** S4

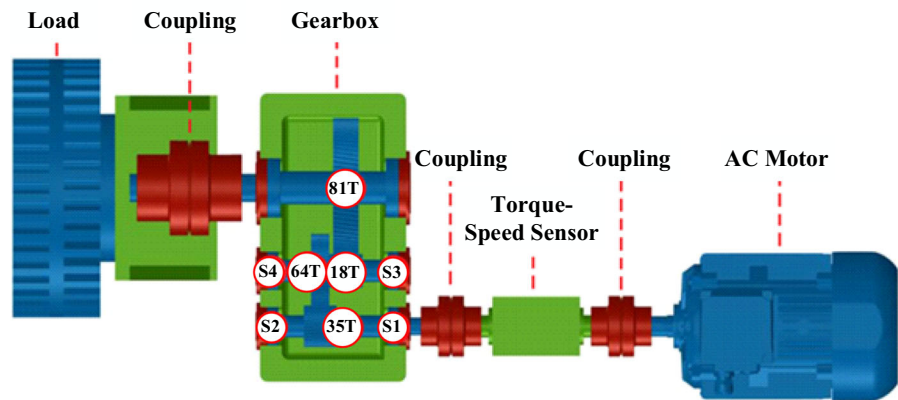
Table 4 The amplitudes and SNRs of the sun gear fault before and after processing by the proposed method

Data source	A_{FFT} (m/s^2)	SNR_{FFT} (dB)
Originally collected data		
S1	1×10^{-3}	- 59.17
S2	3.64×10^{-4}	- 68.00
S3	1.64×10^{-4}	- 74.97
S4	3.89×10^{-4}	- 67.39
After processing by our proposed method		
S1	0.42	- 2.68
S2	0.26	- 2.47
S3	0.07	- 2.50
S4	0.08	- 4.07

asynchronous motor for driving the gearbox and a magnetic powder brake for loading. An NI data acquisition system is employed, including four IEPE accelerometers, a PXI-1031 mainframe, PXI-4472B data acquisition cards and LabVIEW software. In Fig. 8, S1, S2, S3 and S4 are the sensor locations for monitoring the gearbox condition. Additional information on the test rig is provided in Ref. [34].

The single-stage planetary gearbox consists of a sun gear with 13 teeth, 3 planet gears with 64 teeth and a fixed ring gear with 146 teeth. The sun gear, which is mounted on the input shaft and driven by an electric motor, rotates around its own center. The planet gears mesh with the sun gear and ring gear. In addition, the planet gears not only rotate around their own centers but also rotate around the center of the sun gear. A wear tooth fault is implanted on one sun gear tooth.

Fig. 12 Schematic of the fix-axis gearbox test rig



The tooth wear fault is shown in Fig. 9. The fault characteristic frequency is 55.34 Hz, as calculated according to Ref. [34].

The time-domain waveforms, FFT spectra and zoomed spectra of the originally collected condition monitoring data from S1, S2, S3 and S4 are given in Fig. 10. The frequency that has the maximum FFT amplitude (A_{FFT}) is marked by f_{max} . As shown in Fig. 10, the background noise is significant, and the frequencies exist in a wide range. The fault frequency of 55.34 Hz cannot be found directly from the frequency spectra.

The proposed method is used to detect the sun gear fault, and PSO is adopted to optimize the parameters. The basic settings for PSO, which are P_{size} , T_{gen} , C_1 and C_2 , are the same as those in the simulation dataset validation. Other settings are given in Table 3. The stop-band cutoff frequency in the FSRTM is set to 52 Hz, and the rescaling ratio is 600.

The resonated signals from the second VSSNS are given in Fig. 11, where the detected frequencies are 54 Hz (from S1), 54.83 Hz (from S2), 54.83 Hz (from S3) and 55.83 Hz (from S4). These detected frequencies are close to the calculated fault characteristic frequency (55.34 Hz). In this paper, if the absolute frequency error between the fault characteristic

frequency and detected frequency is lower than 2 Hz when considering the vibration impact caused by the operating environment and meshing among components, in addition, the output signal from the second VSSNS shows obvious periodicity. In such a case, the detected frequency is regarded as the frequency caused by a defective component, and the fault signal is detected. Otherwise, the fault signal is not detected. As shown in Fig. 11, the output signal shows obvious periodicity, and the frequency of the fault signal is exposed. The amplitude and SNR of the fault signal are listed in Table 4. In Table 4, the amplitudes and SNRs of the sun gear fault from our proposed method are derived by order of magnitude compared with the originally collected data.

3.3 Validation by a fixed-axis gearbox test rig

Bearings are typical components in rotating machines. A bearing with several naturally developed faults is used to validate our proposed method. The fault signal is collected from a fixed-axis gearbox test rig. It is widely accepted that a weak naturally developed fault is hard to detect because the characteristic fault frequencies related to the damage are usually submerged in heavy background noise due to the meshing

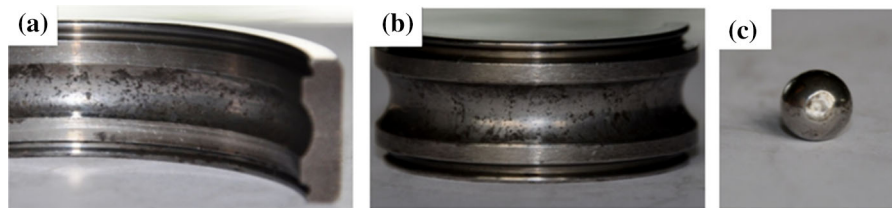


Fig. 13 The faults on the right-hand bearing mounted on the HS shaft: **a** the outer race faults, **b** the inner race faults and **c** the ball faults

Table 5 The fault characteristic frequencies of bearings in the test rig

Shaft	Bearing type	BPFO (Hz)	BPFI (Hz)	BSF (Hz)	FTF (Hz)
HS	SKF 6205	71.70	108.30	47.17	7.96
LS	SKF 6208	8.70	13.19	5.68	0.96

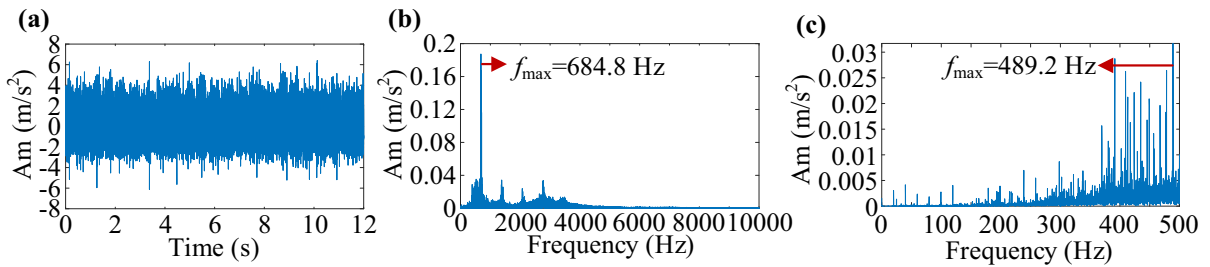


Fig. 14 a Time-domain waveform, b FFT spectrum and c zoomed spectrum of the collected data from S1 on a fixed-axis gearbox

gears. The background noise contains abundant disturbance frequencies that may be generated due to the faults on other components, the meshing among components, and the vibration of an input shaft or the operational conditions. The SNR of a weak naturally developed fault is usually very small.

The information for the fixed-axis gearbox test rig is referenced in Ref. [9]. The test rig shown in Fig. 12 includes a two-stage fixed-axis gearbox, a 4-kW three-phase asynchronous motor for driving the gearbox and adjusting different speeds and a magnetic powder brake for loading. In the gearbox, there are three shafts: a high-speed (HS), intermediate-speed (IS) and low-speed (LS) shaft. The gear, which has 81 teeth mounted on the LS shaft, is meshed with a gear with 18 teeth mounted on the IS shaft. Another gear with 64 teeth mounted on the IS shaft is meshed with a gear with 35 teeth mounted on the HS shaft. The HS and IS shafts are supported by SKF 6205 bearings, and the LS shaft is supported by SKF 6208 bearings.

The positions of the sensors are marked as S1, S2, S3 and S4. The NI data acquisition system is adopted, including four IEPE accelerometers, a PXI-1031 mainframe, PXI-4472B data acquisition cards and LabVIEW software. The experimental conditions are as follows: 20 Hz HS rotation, 20 kHz signal vibration sampling frequency, 12 s sampling duration with two different loads: 199 Nm and 405 Nm.

After the data acquisition, all the bearings and gears have faults at different levels. The bearings that are mounted on the HS shaft have many outer race damages. In addition, the inner race damages and ball damages presented simultaneously on the right-hand bearing. These damages are illustrated in Fig. 13. Due to the presence of three types of damage on different elements of a bearing simultaneously, the bearing mounted on the right-hand side of the HS shaft is selected. Therefore, the data collected from the S1 position are used to validate the proposed method. S1 is close to the source of the bearing faults.

Table 6 The FFT amplitudes and SNRs of the bearing faults before and after processing by the proposed method

Data source	Fault	A_{FFT} (m/s ²)	SNR _{FFT} (dB)
From originally collected data	BPFO	2.83×10^{-5}	- 89.97
	BPFI	7.07×10^{-5}	- 82.01
	BSF	6.35×10^{-5}	- 82.93
After the proposed VR	BPFO	0.17	- 2.02
	BPFI	0.38	- 3.28
	BSF	0.43	- 0.62

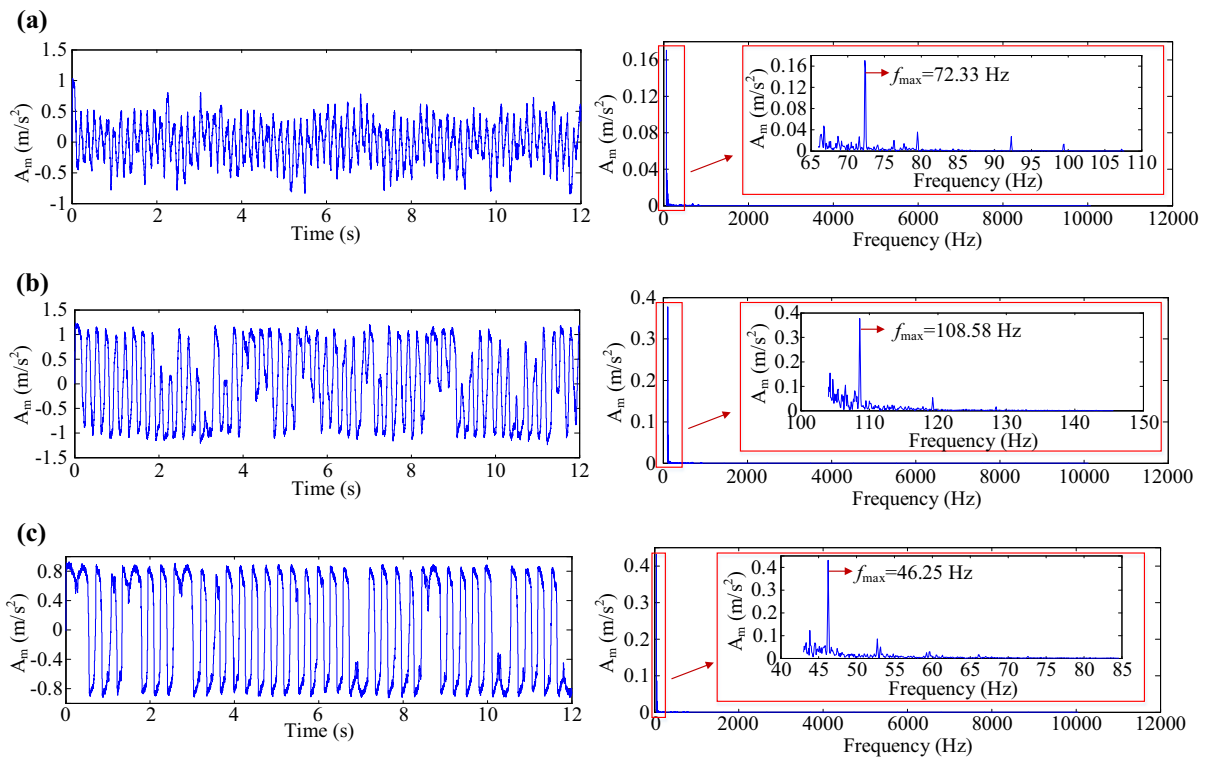


Fig. 15 The time-domain waveforms and frequency spectra of the detected signals for **a** BPFO, **b** BPFI and **c** BSF

The characteristic frequencies of the bearing faults can be calculated according to Ref. [35]. The calculation of fault characteristic frequencies is given in Eq. (23), and the results are listed in Table 5. In Table 5, BPFO, BPFI, BSF and FTF represent the ball pass frequency outer race, ball pass frequency inner race, ball spin frequency and fundamental train frequency, respectively.

$$\begin{cases} f_{BPFO} = \frac{N_B}{2} F_R \left(1 - \frac{D_B \cos(\theta)}{D_P} \right) \\ f_{BPFI} = \frac{N_B}{2} F_R \left(1 + \frac{D_B \cos(\theta)}{D_P} \right) \\ f_{BSF} = \frac{D_P}{D_B} F_R \left(1 - \frac{D_B^2 \cos^2(\theta)}{D_P^2} \right) \\ f_{FTF} = \frac{1}{2} F_R \left(1 - \frac{D_B \cos(\theta)}{D_P} \right) \end{cases} \quad (23)$$

In Eq. (23), N_B is the number of rolling elements in a bearing, F_R is the shaft speed, D_B is the ball diameter, D_P is the pitch diameter and θ is the ball contact angle.

The originally collected data from S1 are used for validation. The time-domain waveform and FFT spectrum of the collected data from S1 are shown in

Fig. 14, where the fault characteristic frequencies are totally lost in the disturbance frequencies. However, the gear meshing frequency (F_{mesh}) and its harmonics are obvious. F_{mesh} refers to the meshing of gears mounted on the HS and IS shafts. This can be calculated according to the rotating speed of a gear (R_s) and its tooth number (N_T) as Eq. (24). According to Eq. (24), $F_{mesh} = 700$ Hz.

$$F_{mesh} = R_s \times N_T \quad (24)$$

PSO is used to optimize the parameters. The settings for PSO are the same as those when using the planetary gearbox dataset for validation. When adopting FSRTM, the stop-band cutoff frequencies for the three types of faults are set as follows: 66 Hz (for BPFO), 104 Hz (for BPFI) and 43 Hz (for BSF). The rescaling ratio is 600. The detection results are given in Table 6.

The detected frequencies are 72.33 Hz, 108.58 Hz and 46.25 Hz. These detected frequencies are close to the calculated fault characteristic frequencies when considering the vibrational circumstances; therefore,

Table 7 Detection results of the implanted sun gear fault under different scenarios

Fault characteristic frequency (Hz)	Scenario	Sensor	Detected frequency (Hz)	A_{FFT} (m/s ²)	SNR_{FFT} (dB)	Iteration epochs
$F_{gear} = 55.34$	Scenario 1	S1	54	0.22	- 4.32	29
		S2	54.83	0.01	- 7.67	21
		S3	79.45	0.01	- 10.86	22
		S4	241.50	0.02	- 11.97	37
	Scenario 2	S1	54	0.28	- 4.03	35
		S2	54.83	0.01	- 7.96	24
		S3	54.83	0.02	- 6.03	41
		S4	241.50	0.02	- 10.81	23
	Scenario 3	S1	104	0.07	- 11.37	39
		S2	54.83	0.02	- 7.63	65
		S3	54.83	0.02	- 6.05	57
		S4	241.50	0.02	- 11.04	39
	Scenario 4	S1	54	0.54	- 4.40	75
		S2	54.83	0.08	- 7.20	78
		S3	54.83	0.10	- 5.91	53
		S4	55.83	0.06	- 8.89	53
	Scenario 5	S1	54	0.93	- 3.62	103
		S2	54.83	0.10	- 4.80	58
		S3	54.83	0.35	- 1.64	77
		S4	55.83	0.07	- 4.46	52

Table 8 Detection results of the naturally developed bearing faults under different scenarios

Fault characteristic frequency (Hz)	Scenario	Fault	Detected frequency (Hz)	A_{FFT} (m/s ²)	SNR_{FFT} (dB)	Iteration epochs
$F_{BPFO} = 71.70$	Scenario 1	BPFO	66.25	0.02	- 12.17	22
		BPFI	108.58	0.02	- 10.36	23
		BSF	46.25	0.05	- 3.27	45
$F_{BPFI} = 108.30$	Scenario 2	BPFO	72.33	0.02	- 11.01	41
		BPFI	108.58	0.03	- 8.34	37
		BSF	46.25	0.05	- 2.23	40
$F_{BSF} = 47.17$	Scenario 3	BPFO	72.33	0.02	- 10.97	41
		BPFI	108.58	0.03	- 8.32	30
		BSF	46.25	0.06	- 2.09	37
	Scenario 4	BPFO	72.33	0.07	- 6.42	51
		BPFI	108.58	0.12	- 7.26	51
		BSF	46.25	0.25	- 0.82	63
	Scenario 5	BPFO	72.33	0.18	- 5.44	60
		BPFI	108.58	0.37	- 2.37	58
		BSF	46.25	0.73	0.40	55

the detected frequencies are regarded as the fault frequencies.

The outputs from the second VSSNS are given in Fig. 15, where the output signal shows obvious periodicity compared with the originally collected data (in Fig. 14). In Fig. 14, no fault can be detected directly from the frequency spectrum, but the fault frequencies are obvious from the perspective of the frequency spectrum in Fig. 15. Therefore, the fault frequencies are exposed, and the amplitudes and SNRs are greatly improved.

4 Comparison and discussion

In the proposed method, two VSSNSs are adopted. The background noise and manually injected high-frequency interferences are used to achieve resonance in the first and second VSSNSs, respectively. As

analyzed before, some researchers have successfully detected a target signal using only one nonlinear system based on the VR mechanism. There is no general guidance or theoretical standard on how to determine the number of nonlinear systems. To demonstrate the impacts caused by the number of nonlinear systems on the detection performance, a series of scenarios are considered and compared as follows.

Scenario 1. Only one CBS is adopted, and high-frequency interference is injected.

Scenario 2. Only one VSSNS is adopted, and high-frequency interference is injected.

Scenario 3. Only one VSSNS is adopted, but high-frequency interference is not injected; only the background noise is used for achieving resonance.

Scenario 4. Two CBSs are used, and high-frequency interference is injected; the VSSNSs in our proposed method are replaced by CBSs.

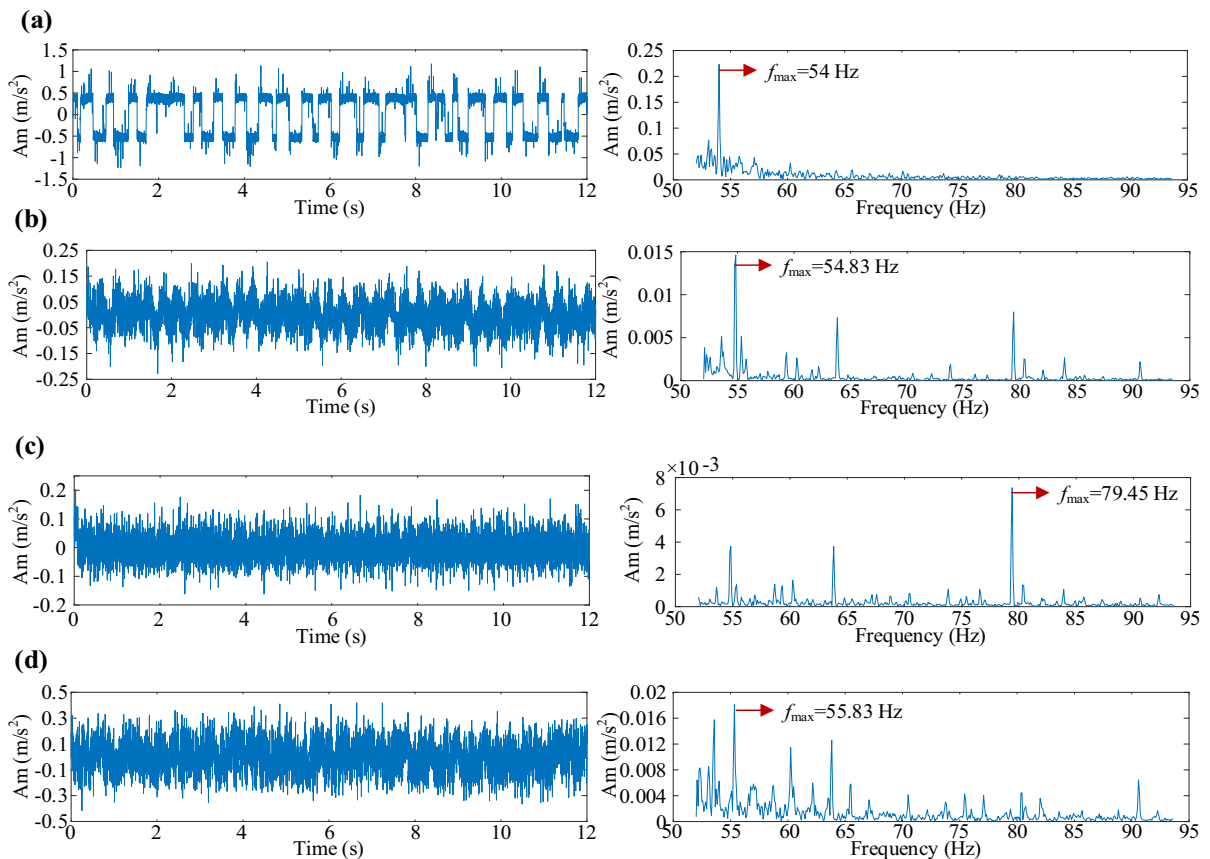


Fig. 16 The time-domain waveforms and zoomed FFT spectra of the output signals from Scenario 1 using the data collected from **a** S1, **b** S2, **c** S3 and **d** S4

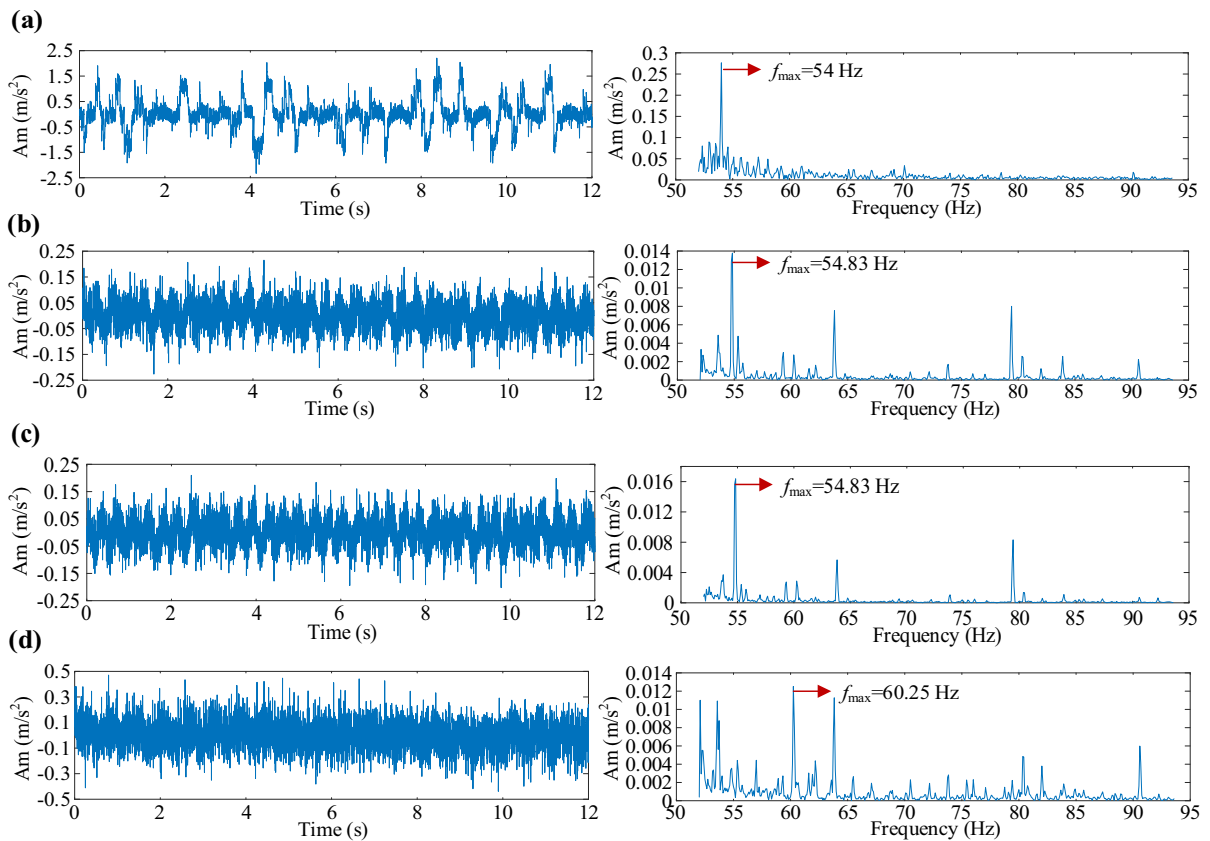


Fig. 17 The time-domain waveforms and zoomed FFT spectra of the output signals from Scenario 2 using the data collected from **a** S1, **b** S2, **c** S3 and **d** S4

Scenario 5. Our proposed method.

In the above five scenarios, datasets for the implanted sun gear fault in the planetary gearbox and the naturally developed bearing faults in the fixed-axis gearbox are used. PSO is adopted to optimize the related parameters. The detection results from the different scenarios are compared in Tables 7 and 8, where F_{gear} , F_{BPFO} , F_{BPFI} and F_{BSF} denote the fault characteristic frequencies, which are calculated according to the operating and shape parameters of a component.

In Tables 7 and 8, the gray color indicates an undetected fault in a scenario. In Tables 7 and 8, all the faults can be detected in Scenarios 4 and 5, which demonstrates that using two nonlinear systems is beneficial for fault detection. From the perspective of A_{FFT} and SNR_{FFT} , the detection results from our proposed method (Scenario 5) are better than those using the CBSs (Scenario 4).

If only one nonlinear system is used, the faults cannot always be detected (Scenarios 1–3 in Table 7 and Scenario 1 in Table 8). In particular, the faults cannot be detected by using only one CBS. The sun gear fault also cannot be detected by using only one VSSNS with or without injected high-frequency interference if the data collected from S4 are used (Scenarios 2 and 3 in Table 7). However, naturally developed bearing faults can be detected by using only one VSSNS with or without injected high-frequency interference (Scenarios 2–3 in Table 8). In Scenario 3 in Table 8, the effectiveness of the background noise on resonance is demonstrated. Even though some faults can be detected by using only one VSSNS with or without injected high-frequency interference, the detection performance is not as good as the performance of our proposed method (Scenario 5) from the perspective of A_{FFT} and SNR_{FFT} .

The positive effect on resonance caused by the background noise is illustrated by comparing Tables 5

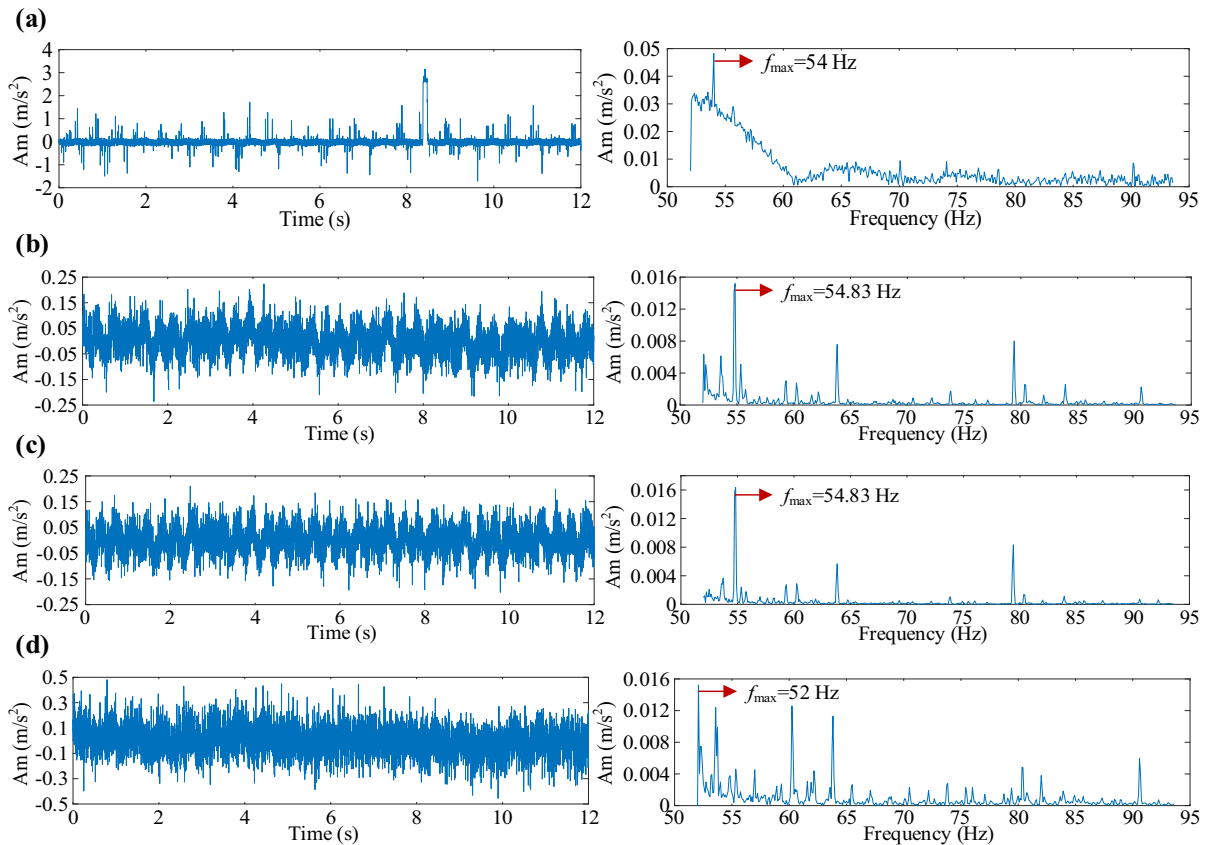


Fig. 18 The time-domain waveforms and zoomed FFT spectra of the output signals from Scenario 3 using the data collected from **a** S1, **b** S2, **c** S3 and **d** S4

and 6 with Tables 7 and 8. In Tables 5 and 6, the SNRs of naturally developed bearing faults are lower than the SNR of the implanted sun gear fault; the background noise in the fixed-axis gearbox is stronger than the noise in the planetary gearbox. However, the naturally developed bearing faults in the fixed-axis gearbox can be detected, and the SNRs are improved more (Scenario 3 in Table 8) than the SNR improvement of the implanted sun gear fault (Scenario 3 in Table 7). The output signals from the last nonlinear systems under different scenarios are given in Figs. 16, 17, 18, 19, 20, 21, 22, 23, 24 and 25, where the frequency with maximum amplitude in the zoomed frequency spectrum is marked by f_{\max} . The output signals in Figs. 16, 17, 18, 19 and 20 focus on the detection of sun gear faults. The output signals in Figs. 21, 22, 23, 24 and 25 focus on the detection of naturally developed bearing faults.

In these zoomed frequency spectra, some faults are not detected under Scenarios 1–3. Even though all the

faults can be detected under Scenarios 4 and 5, the amplitudes of these detected faults under Scenario 4 are lower than the values from our proposed method (Scenario 5). In view of the time-domain waveforms, the output signals still contain considerable background noise with high amplitudes even though the faults are detected under Scenarios 1–3. In addition, the output signals from our proposed method (Scenario 5) show more obvious periodicity in the view of time-domain waveforms than the output signals under Scenario 4.

The barrier height (BH) of a nonlinear system has an important impact on resonance. The BH, which is related to the stability type of a nonlinear system, is determined by the system parameters. Considering the above scenarios, all the faults can be detected in only Scenarios 4 and 5; therefore, the BHs of these nonlinear systems are listed in Tables 9 and 10, where BHs are calculated according to the system parameters of the second nonlinear system.

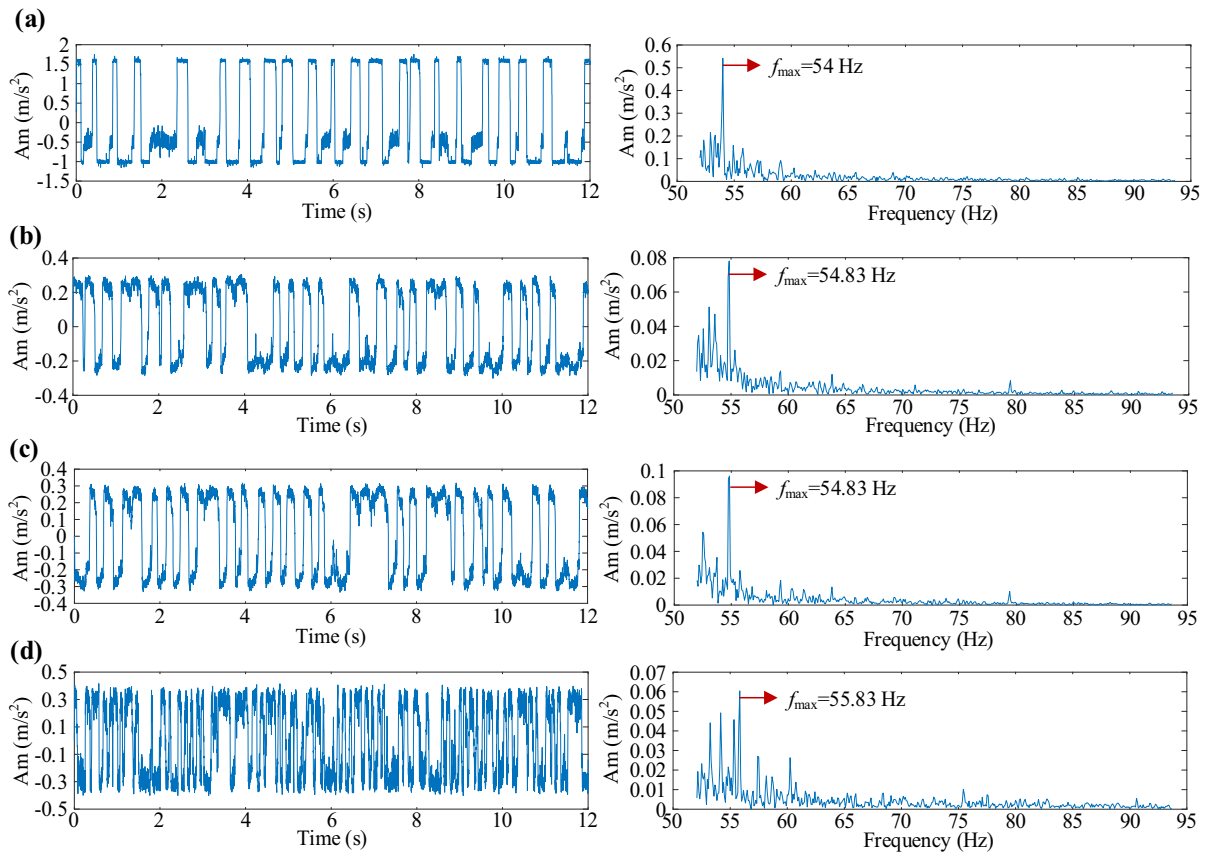


Fig. 19 The time-domain waveforms and zoomed FFT spectra of the output signals from Scenario 4 using the data collected from **a** S1, **b** S2, **c** S3 and **d** S4

In Tables 9 and 10, “–” means that a BH is incalculable due to the stability type. MS, TS and BS stand for monostable, tristable and bistable. During detecting the sun gear fault and bearing faults, the stability type in the second VSSNS can be either MS, BS or TS in Table 9. If the stability type is MS, BH is not necessary for calculation. In Table 10, the second VSSNS can be TS or BS. If parameter b is negative, the stability type in the VSSNS is BS in both Tables 9 and 10. However, negative parameter b is meaningless from the physical view of a CBS. The BH is difficult to calculate if the VSSNS is transformed into BS or TS, but it can be obtained according to the output signal and potential well function. In Tables 9 and 10, even though the BHs in the CBSs are lower than those in the VSSNSs, the detection performance of our proposed method is better in view of the enhancement of A_{FFT} and SNR_{FFT} in a fault signal (regardless of whether the fault is an implanted gear fault or naturally developed

bearing faults). Moreover, the adopted VSSNS provides more probability to achieve resonance by tuning system parameters.

Through all validations, the effectiveness of our proposed method, which focuses on the detection of a high-frequency character signal, is demonstrated. First, our proposed method shows better performance than the VR-based CBS(s) regardless of using only one CBS or cascade CBSs. This is demonstrated in Tables 7 and 8. Second, our proposed method is effectively employed to detect faults on rotating machines, including naturally developed bearing faults and an implanted gear fault. The frequencies of these faults are much greater than 1 Hz. Therefore, our proposed method can overcome the restriction of adiabatic approximation theory. Third, different rotating machines are considered: a fixed-axis gearbox and a planetary gearbox. Fourth, our proposed method shows improvements in amplitude, SNR and

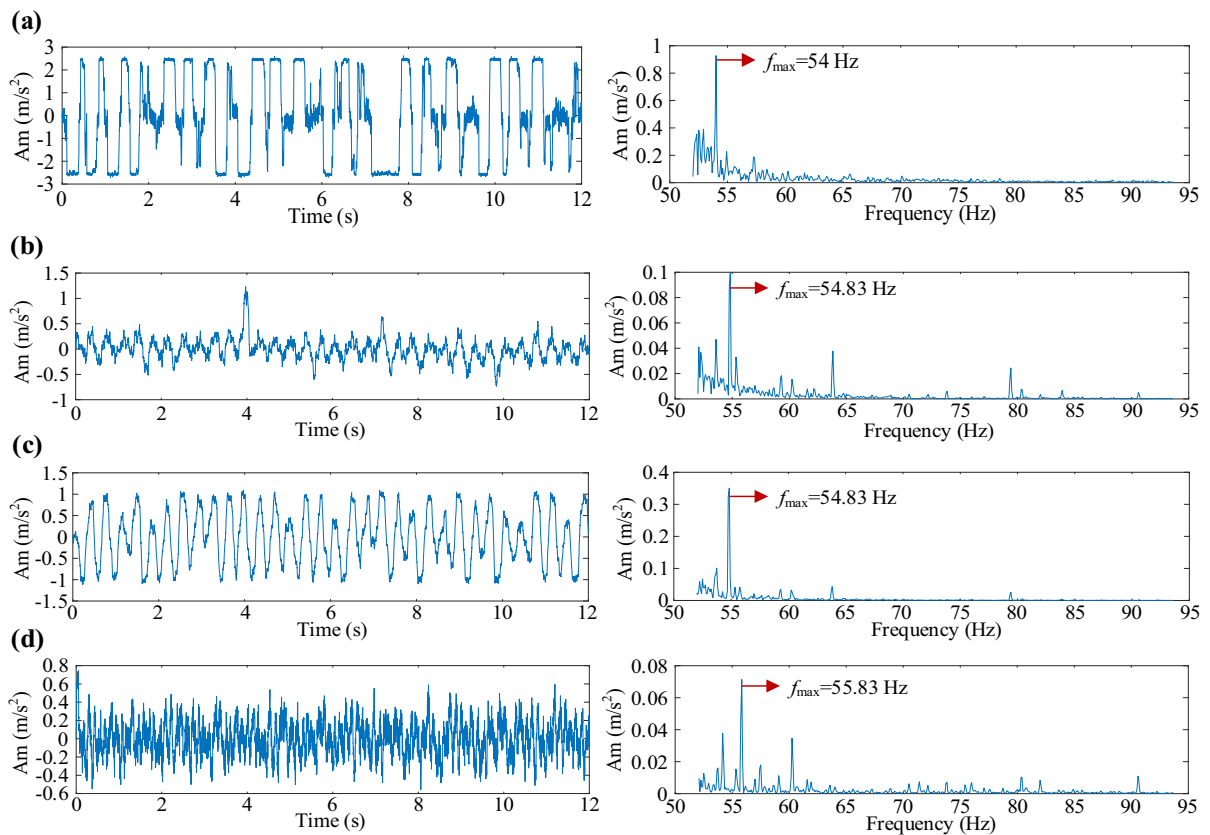


Fig. 20 The time-domain waveforms and zoomed FFT spectra of the output signals from Scenario 5 using the data collected from **a** S1, **b** S2, **c** S3 and **d** S4

periodicity of the detected signals, which is demonstrated in Tables 7 and 8 and Figs. 16, 17, 18, 19, 20, 21, 22, 23, 24 and 25. Fifth, the VSSNS can be transferred into MS, BS or TS by tuning the system parameters; therefore, the possibility of resonance achievement is gained. Sixth, even though some faults can be detected by using only one nonlinear system, the detection performance is insufficient. There are still many disturbance frequencies with high FFT amplitudes, and the time-domain waveform of a resonated signal shows less periodicity than the one from our proposed method. Last, the background noises are not always undesirable; they are beneficial to resonance in the proposed method.

5 Conclusions

In this paper, a detection method for a high-frequency character signal is proposed based on the VR

mechanism and cascaded VSSNSs. In this method, the background noise is used rather than suppressed, which is different from existing noise cancellation methods. The stability type of a VSSNS can be easily and adaptively changed into MS, BS or TS by tuning the system parameters. To deploy the VR mechanism, the background noise, which has been mixed when collecting data from the sensors, and the manually injected high-frequency interference are used to achieve resonance for the two cascaded VSSNSs. To achieve adaptive detection and optimization, the parameters related to the nonlinear systems and the injected high-frequency interferences are optimized by PSO. Through a validation conducted on the simulation dataset and rotating machines, the good performance of our proposed method is demonstrated in terms of the enhancement on FFT amplitude, SNR and periodicity of a resonated signal.

The main contribution of this paper is that a new VR configuration is constructed for detecting a high-

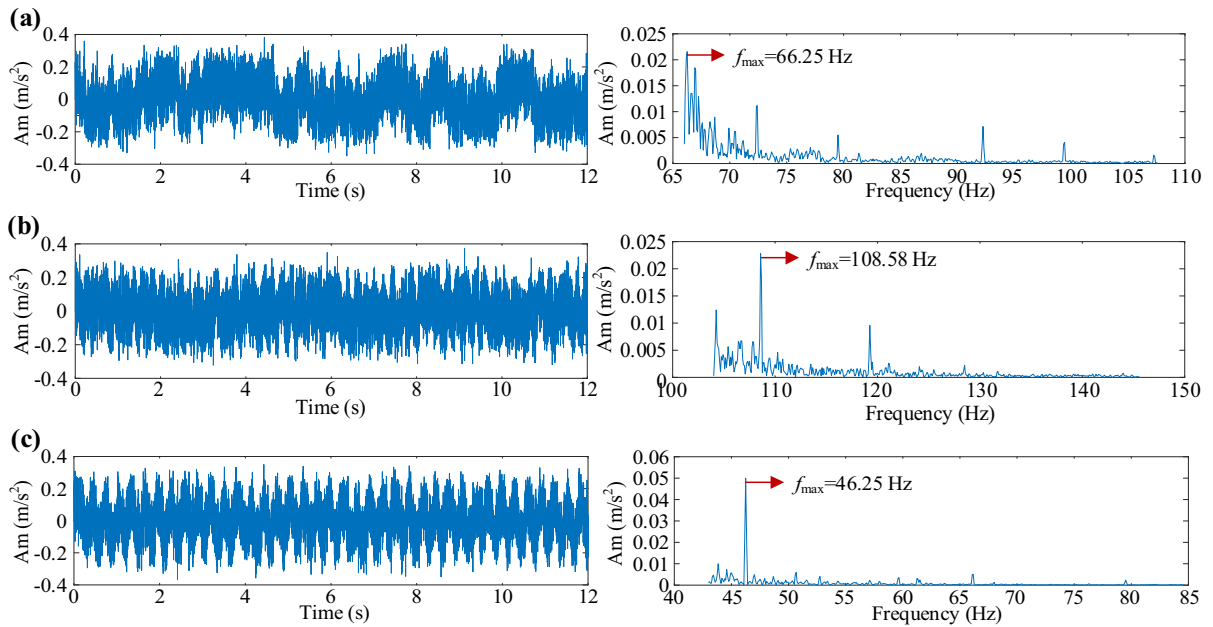


Fig. 21 The time-domain waveforms and zoomed frequency spectra of the output signals from Scenario 1 for detecting **a** BPFO, **b** BPFI and **c** BSF

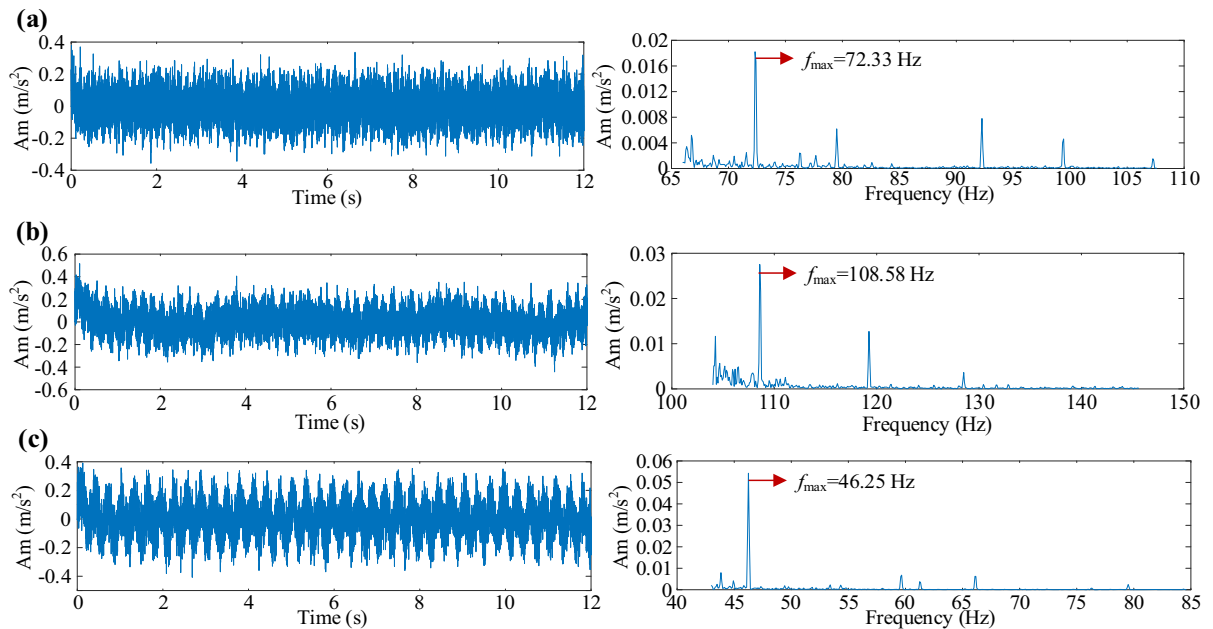


Fig. 22 The time-domain waveforms and zoomed frequency spectra of the output signals from Scenario 2 for detecting **a** BPFO, **b** BPFI and **c** BSF

frequency character signal, and its application is extended into mechanical industry. The classic VR is always restricted by the adiabatic approximation theory, which cannot be directly applied to weak fault

detection because the fault character frequency of a rotating machine is always greater than 1 Hz, especially under operating conditions. In this paper, our proposed method has successfully detected faults on

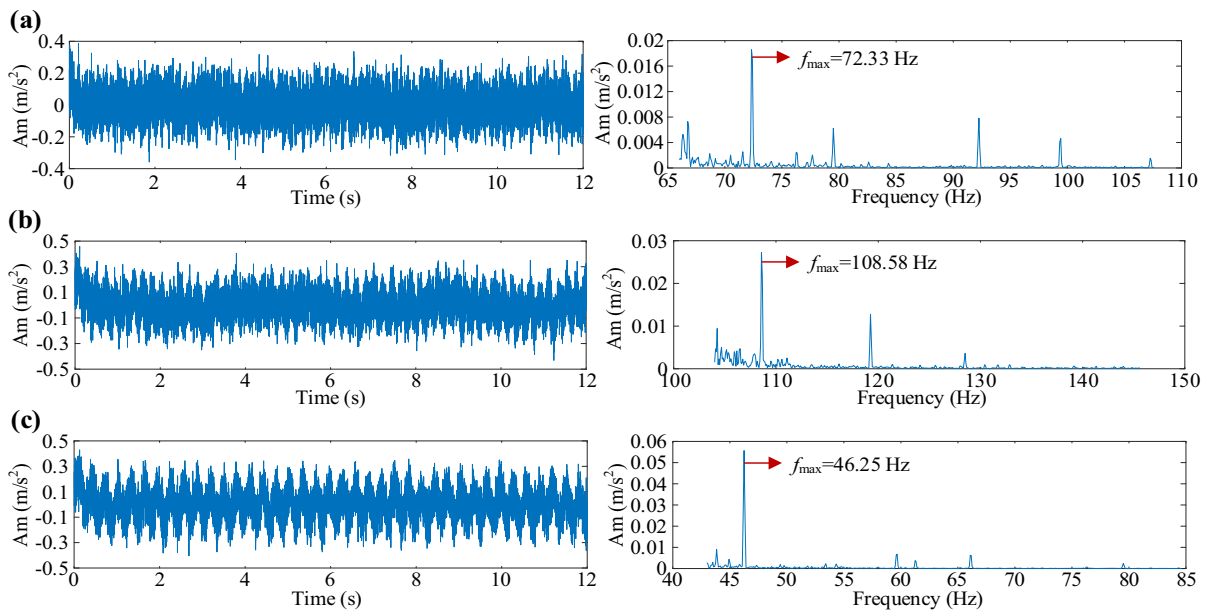


Fig. 23 The time-domain waveforms and zoomed frequency spectra of the output signals from Scenario 3 for detecting **a** BPFO, **b** BPFI and **c** BSF

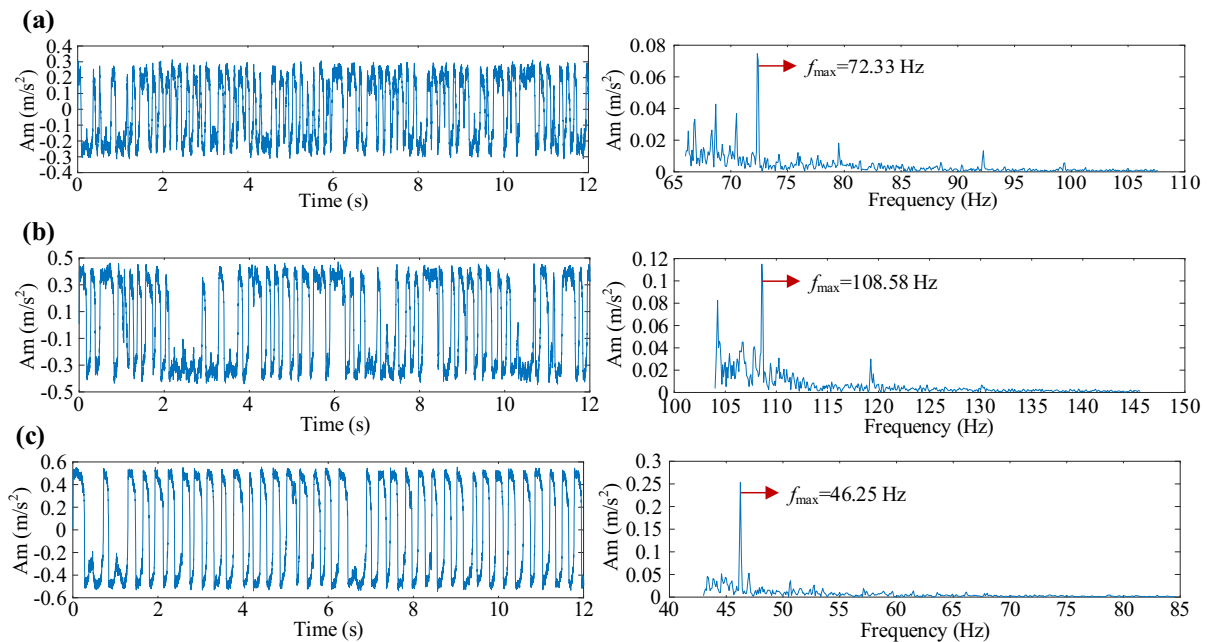


Fig. 24 The time-domain waveforms and zoomed frequency spectra of the output signals from Scenario 4 for detecting **a** BPFO, **b** BPFI and **c** BSF

two typical rotating machines: a bearing and a gear. In addition, two common gearboxes, a planetary gearbox and a fixed-axis gearbox, are considered.

The frequency transform with respect to a high-frequency signal mainly depends on FSRTM, which is more effective if a fault characteristic frequency is known in advance. If the fault characteristic frequency

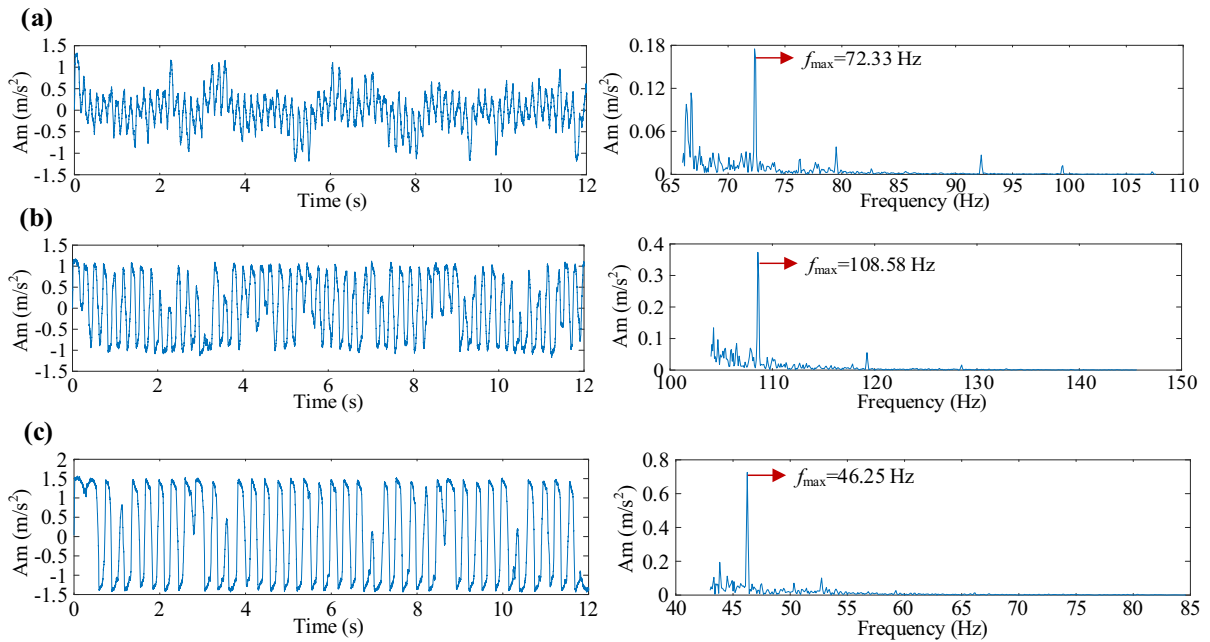


Fig. 25 The time-domain waveforms and zoomed frequency spectra of the output signals from Scenario 5 for detecting **a** BPFO, **b** BPFI and **c** BSF

Table 9 The stability types and BHs of the second nonlinear system when detecting the sun gear fault in Scenarios 4–5

Sensor	VSSNS		CBS				
	<i>a</i>	<i>b</i>	Stable type	BH	<i>a_c</i>	<i>b_c</i>	BH
S1	19.24	1.18	MS	–	1.02	0.81	0.32
S2	9.87	0.15	TS	0.04	0.48	9.97	5.8×10^{-3}
S3	24.35	0.16	TS	0.22	0.38	6.68	5.4×10^{-3}
S4	26.49	0.30	TS	0.19	0.30	5.54	4.1×10^{-3}

Table 10 The stability types and BHs of the second nonlinear system when detecting the naturally developed bearing fault in Scenarios 4–5

Fault	VSSNS				CBS		
	<i>a</i>	<i>b</i>	Stable type	BH	<i>a_c</i>	<i>b_c</i>	BH
BPFO	13.40	0.20	TS	0.06	0.17	7.20	1.0×10^{-3}
BPFI	1.49	– 0.04	BS	0.01	0.27	3.16	5.8×10^{-3}
BSF	4.59	– 0.08	BS	0.05	0.47	2.71	0.02

is unknown in advance, the parameter related to the frequency shift in the FSRTM is hard to set, and the performance of the frequency transform may be impacted. In the future, we will adopt a more effective frequency transform method in which the characteristic frequency is not necessary.

Acknowledgements The authors gratefully acknowledge support from the National Natural Science Foundation of China (52075094, 51705321), the Fundamental Research Funds for the Central Universities (2232019D3-29), the China Postdoctoral Science Foundation (2017M611576) and the Initial Research Funds for Young Teachers of Donghua University.

Compliance with ethical standards

Conflict of interest The authors declare that they have no conflicts of interest.

References

- Landa, P.S., McClintock, P.V.E.: Vibrational resonance. *J. Phys. A Math. Gen.* **33**, L433–L438 (2000)
- Liu, H.G., Liu, X.L., Yang, J.H., Sanjuán, M.A.F., Cheng, G.: Detecting the weak high-frequency character signal by vibrational resonance in the Duffing oscillator. *Nonlinear Dyn.* **89**, 2621–2628 (2017)
- Tan, J., Chen, X., Wang, J., Chen, H., Cao, H., Zi, Y., He, Z.: Study of frequency-shifted and re-scaling stochastic resonance and its application to fault diagnosis. *Mech. Syst. Signal Process.* **23**, 811–822 (2009)
- Wang, J., He, Q., Kong, F.: Adaptive multiscale noise tuning stochastic resonance for health diagnosis of rolling element bearings. *IEEE Trans. Instrum. Meas.* **64**, 564–577 (2015)
- Elforjani, M., Bechhoefer, E.: Analysis of extremely modulated faulty wind turbine data using spectral kurtosis and signal intensity estimator. *Renew. Energy* **127**, 258–268 (2018)
- He, D., Wang, X., Li, S., Lin, J., Zhao, M.: Identification of multiple faults in rotating machinery based on minimum entropy deconvolution combined with spectral kurtosis. *Mech. Syst. Signal Process.* **81**, 235–249 (2016)
- Li, Y., Xu, M., Liang, X., Huang, W.: Application of bandwidth EMD and adaptive multiscale morphology analysis for incipient fault diagnosis of rolling bearings. *IEEE Trans. Ind. Electron.* **64**, 6506–6517 (2017)
- Qin, Y., Mao, Y., Tang, B.: Multicomponent decomposition by wavelet modulus maxima and synchronous detection. *Mech. Syst. Signal Process.* **91**, 57–80 (2017)
- Zhang, X., Zhao, J., Bajrić, R., Wang, L.: Application of the DC offset cancellation method and S transform to gearbox fault diagnosis. *Appl. Sci.* **7**, 207 (2017)
- Liu, J., Shao, Y.: Overview of dynamic modelling and analysis of rolling element bearings with localized and distributed faults. *Nonlinear Dyn.* **93**, 1765–1798 (2018)
- Chan, J.C.L., Tan, C.P., Trinh, H.: Robust fault reconstruction for a class of infinitely unobservable descriptor systems. *Int. J. Syst. Sci.* **48**, 1646–1655 (2017)
- Chan, J.C.L., Tan, C.P., Trinh, H., Kamal, M.A.S., Chiew, Y.S.: Robust fault reconstruction for a class of non-infinitely observable descriptor systems using two sliding mode observers in cascade. *Appl. Math. Comput.* **350**, 78–92 (2019)
- Qiao, Z., Lei, Y., Lin, J., Jia, F.: An adaptive unsaturated bistable stochastic resonance method and its application in mechanical fault diagnosis. *Mech. Syst. Signal Process.* **84**, 731–746 (2017)
- Zhang, S., Yang, J., Zhang, J., Liu, H., Hu, E.: On bearing fault diagnosis by nonlinear system resonance. *Nonlinear Dyn.* **98**, 2035–2052 (2019)
- Li, J., Zhang, J., Li, M., Zhang, Y.: A novel adaptive stochastic resonance method based on coupled bistable systems and its application in rolling bearing fault diagnosis. *Mech. Syst. Signal Process.* **114**, 128–145 (2019)
- Dong, H., Wang, H., Shen, X., Jiang, Z.: Effects of second-order matched stochastic resonance for weak signal detection. *IEEE Access* **6**, 46505–46515 (2018)
- Zhang, G., Zhang, Y., Zhang, T., Xiao, J.: Stochastic resonance in second-order underdamped system with exponential bistable potential for bearing fault diagnosis. *IEEE Access* **6**, 42431–42444 (2018)
- Lai, Z.H., Liu, J.S., Zhang, H.T., Zhang, C.L., Zhang, J.W., Duan, D.Z.: Multi-parameter-adjusting stochastic resonance in a standard tri-stable system and its application in incipient fault diagnosis. *Nonlinear Dyn.* **96**, 2069–2085 (2019)
- Lu, S., He, Q., Wang, J.: A review of stochastic resonance in rotating machine fault detection. *Mech. Syst. Signal Process.* **116**, 230–260 (2019)
- Qiao, Z., Lei, Y., Li, N.: Applications of stochastic resonance to machinery fault detection: a review and tutorial. *Mech. Syst. Signal Process.* **122**, 502–536 (2019)
- Duan, F., Chapeau-Blondeau, F., Abbott, D.: Double-maximum enhancement of signal-to-noise ratio gain via stochastic resonance and vibrational resonance. *Phys. Rev. E* **90**, 022134 (2014)
- Xiao, L., Zhang, X., Lu, S., Xia, T., Xi, L.: A novel weak-fault detection technique for rolling element bearing based on vibrational resonance. *J. Sound Vib.* **438**, 490–505 (2019)
- Baltanás, J.P., López, L., Blechman, I.I., Landa, P.S., Zaikin, A., Kurths, J., Sanjuán, M.A.F.: Experimental evidence, numerics, and theory of vibrational resonance in bistable systems. *Phys. Rev. E Stat. Nonlinear Soft Matter Phys.* **67**, 066119 (2003)
- Zaikin, A.A., López, L., Baltanás, J.P., Kurths, J., Sanjuán, M.A.F.: Vibrational resonance in a noise-induced structure. *Phys. Rev. E Stat. Nonlinear Soft Matter Phys.* **66**, 011106 (2002)
- Ullner, E., Zaikin, A., Garcia-Ojalvo, J., Bascónes, R., Kurths, J.: Vibrational resonance and vibrational propagation in excitable systems. *Phys. Lett. A* **312**, 348–354 (2003)
- Yao, C., He, Z., Nakano, T., Qian, Y., Shuai, J.: Inhibitory-autapse-enhanced signal transmission in neural networks. *Nonlinear Dyn.* **97**, 1425–1437 (2019)
- Chizhevsky, V.N., Smeu, E., Giacomelli, G.: Experimental evidence of “Vibrational resonance” in an optical system. *Phys. Rev. Lett.* **91**, 220602 (2003)
- Chizhevsky, V.N., Giacomelli, G.: Improvement of signal-to-noise ratio in a bistable optical system: comparison between vibrational and stochastic resonance. *Phys. Rev. A* **71**, 011801(R) (2005)
- Gao, J., Yang, J., Huang, D., Liu, H., Liu, S.: Experimental application of vibrational resonance on bearing fault diagnosis. *J. Braz. Soc. Mech. Sci. Eng.* **41**, 1–13 (2019)
- Liu, Y., Dai, Z., Lu, S., Liu, F., Zhao, J., Shen, J.: Enhanced bearing fault detection using step-varying vibrational resonance based on duffing oscillator nonlinear system. *Shock Vib.* **2017**, 1–14 (2017)
- Rajasekar, S., Sanjuan, M.A.F.: *Nonlinear Resonances*. Springer, Berlin (2016)

32. Ren, Y., Duan, F.: Theoretical and experimental implementation of vibrational resonance in an array of hard limiters. *Physica A Stat. Mech. Appl.* **456**, 319–326 (2016)
33. Xiao, L., Tang, J., Zhang, X., Xia, T.: Weak fault detection in rotating machineries by using vibrational resonance and coupled varying-stable nonlinear systems. *J. Sound Vib.* **478**, 115355 (2020)
34. Zhang, X., Kang, J., Bechhoefer, E., Zhao, J.: A new feature extraction method for gear fault diagnosis and prognosis. *Eksploat. Niezawodn. Maint. Reliab.* **16**, 295–300 (2014)
35. Randall, R.B., Antoni, J.: Rolling element bearing diagnostics—a tutorial. *Mech. Syst. Signal Process.* **25**, 485–520 (2011)

Publisher's Note Springer Nature remains neutral with regard to jurisdictional claims in published maps and institutional affiliations.